Monthly Notices
of the
ROYAL ASTRONOMICAL SOCIETY

MNRAS **544,** 2296–2315 (2025) https://doi.org/10.1093/mnras/staf1708
Advance Access publication 2025 October 10

Quasi-periodic pulsations driven by structural oscillations in a kink-unstable flaring coronal loop

J. Stewart,[1]★ P. K. Browning[1] and M. Gordovskyy[2]
[1]*Jodrell Bank Centre for Astrophysics, University of Manchester, Manchester M13 9PL, UK*
[2]*Centre for Astrophysics Research, University of Hertfordshire, Hatfield AL10 9AB, UK*

Accepted 2025 September 30. Received 2025 September 23; in original form 2025 March 4

ABSTRACT

Twisted coronal loops in the solar atmosphere may become kink unstable when their magnetic field lines are sufficiently twisted. This instability can trigger magnetic reconnection, leading to the emission of electromagnetic radiation, which manifests as a solar flare. Previous research has demonstrated that oscillations in microwave emissions, resembling observed quasi-periodic pulsations, can be generated by the reconnecting loop. Our aim is to investigate the relationship between the oscillations of the loop and these microwave pulsations. Using 3D magnetohydrodynamical simulations, we examine two models: a straight loop in a uniform-density atmosphere and a curved loop in a gravitationally stratified atmosphere. Using a new methodology, we extract the reconnecting loop-top from both models and identify structural oscillations. We then compare these oscillations with the gyrosynchrotron (GS) radiation emitted from the simulations, which is forward modelled using a radiative transfer code. We find that oscillations in the GS emissions are driven by sausage- and kink-mode oscillations. However, the relationship between the oscillation frequencies of the GS emission and the identified loop oscillation modes is complex. The dominant mode in the former may result from interference between sausage-mode and kink-mode oscillations or entirely different mechanisms. Results such as these increase our understanding of the time-dependent behaviour of solar flares and lay the groundwork for potential diagnostic tools that could be used to determine physical parameters within a flaring loop.

Key words: magnetic reconnection – MHD – plasmas – Sun: corona – Sun: magnetic fields – Sun: oscillations.

1 INTRODUCTION

It is widely accepted that solar flares are the manifestation of emitted electromagnetic radiation resulting from a release of stored magnetic energy in complex magnetic structures within the solar corona through magnetic reconnection (L. Fletcher et al. 2011; A. O. Benz 2017). Reconnection can be triggered when these structures interact with each other, themselves, or with their surrounding magnetic field (E. Priest 1982; K. Shibata & T. Magara 2011). This mechanism rearranges the magnetic field and releases energy. Consequently, hot plasma and accelerated particles emit radiation across the electromagnetic spectrum out of the flaring region. Solar flares are also associated with coronal mass ejections (CMEs) and the release of energetic particles from the Sun. They play a significant role in the dynamics of the solar wind and space weather (N. Meyer-Vernet 2007; A. A. Vidotto 2021). They can vary in duration, ranging from a few minutes to several hours (L. Fletcher et al. 2011; A. O. Benz 2017), and their intensity and frequency of occurrence vary with the solar cycle (D. H. Hathaway 2010).

Quasi-periodic pulsations (QPPs), short-lived oscillations, are frequently detected in flare emissions in various wavelengths. The earliest documentation of these oscillations can be dated back to a review on solar continuum bursts written by A. R. Thompson & A. Maxwell (1962). However, it was G. K. Parks & J. R. Winckler (1969) who initially drew attention to these oscillations by highlighting a 16-s modulation in the X-ray intensity–time profile of a 1968 solar flare. Since then, the presence of QPPs in solar flares has been consistently recorded. In a review by A. R. Inglis et al. (2016), a 30 per cent detection rate of QPPs was reported in 675 GOES (Geostationary Operational Environmental Satellite) M- and X-class flares observed between 2011 and 2016. Subsequently, M. Dominique et al. (2018) reported a 90 per cent detection rate of QPPs within the EUV (extreme ultraviolet) and SXR (soft X-ray) bands among 90 flares detected during solar cycle 24. Further research has shed light on the properties and potential theoretical mechanisms governing QPP emissions. Statistical studies indicate that QPPs exhibit a range of durations, typically lasting between a few seconds and several minutes (I. V. Zimovets et al. 2021) with some briefer QPP events (T. Takakura et al. 1983) and longer lasting oscillations (such as one lasting for over 30 min; T. Zaqarashvili et al. 2013), being observed. QPPs have been observed in stellar flares (M. Mathioudakis et al. 2003, 2006; U. Mitra-Kraev et al. 2005) and pre-main-sequence star flares (F. Reale et al. 2018).

Advances in QPP detection techniques, outlined by A.-M. Broomhall et al. (2019), have unveiled a diverse array of temporal behaviours exhibited by QPPs. These include aperiodic trends, anharmonic shapes, modulated periods and amplitudes, and QPPs superimposed with background noise. The variability observed

---

★ E-mail: jamie.stewart@hse.gov.uk

in QPP periods and temporal behaviours, coupled with the different electromagnetic signatures they exhibit, hints at the existence of multiple QPP driving mechanisms at play within a flaring region. A comprehensive summary of the current understanding of QPPs, including their observation and their theoretical driving mechanisms, can be found in recent reviews by J. A. McLaughlin et al. (2018), V. M. Nakariakov et al. (2019), T. van Doorsselaere et al. (2020), and I. V. Zimovets et al. (2021).

Developing our understanding of QPPs holds great potential. Primarily, gaining insight into the driving mechanisms behind QPPs will contribute to a more comprehensive understanding of the time-dependent nature of energy release in flares, an area that has historically not been fully understood. Furthermore, some QPP oscillations have been shown to exhibit a strong correlation with the background parameters of the flaring plasma, such as temperature, magnetic field strength, and plasma density. For example, K. Karampelas et al. (2023) identified a quantitative relationship between the period of the waves propagating away from a region undergoing oscillatory reconnection and the aforementioned plasma parameters. Oscillatory reconnection has previously been studied as a candidate mechanism for QPP generation (J. A. McLaughlin et al. 2009, 2012, 2018; J. O. Thurgood, D. I. Pontin & J. A. McLaughlin 2017, 2018; V. M. Nakariakov et al. 2019; T. van Doorsselaere et al. 2020; K. Karampelas et al. 2022, 2023; J. Stewart, P. K. Browning & M. Gordovskyy 2022). As such, this indicates that it is possible to develop seismological tools capable of deducing plasma parameters of a flaring region from QPP data.

One important structure related to flares and QPPs is the twisted coronal loop, which can be modelled as a magnetic flux rope. These structures, ubiquitous throughout the corona, are common sources of solar flares (L. Fletcher et al. 2011). Coronal loops may acquire twist, originating from sunspot rotation or subphotospheric motions before they emerge from the photosphere, resulting in the formation of a twisted coronal loop (K. J. H. Phillips 1995; Y. Fan 2009; V. Archontis, A. W. Hood & K. Tsinganos 2013). Oscillations manifest in these loops during reconnection, including kink-mode oscillations, characterized by lateral swaying, sausage-mode oscillations, involving radial expansion and contraction of the loop, and other oscillations such as torsional, fluting, or acoustic modes (V. M. Nakariakov & E. Verwichte 2005; I. De Moortel & V. M. Nakariakov 2012; V. M. Nakariakov et al. 2016). Previous research points to a potential correlation between these oscillations and the occurrence of QPPs in solar flare data (V. Nakariakov, V. Melnikov & V. Reznikova 2003; D. Li et al. 2020; T. I. Kaltman & E. G. Kupriyanova 2023), though recent observational data suggest that this does not apply to all flaring loops (F. Shi et al. 2023).

Kink-unstable twisted coronal loops have long been considered a driving mechanism of solar flares and CMEs (A. W. Hood & E. R. Priest 1979; T. Török & B. Kliem 2005; A. K. Srivastava et al. 2010; P. Kumar et al. 2012). In ideal magnetohydrodynamic (MHD), this occurs when the twist of the magnetic lines within a magnetic flux rope surpasses a critical value, resulting in a breakdown of equilibrium, loop deformation, and magnetic reconnection, ultimately leading to a flare (A. W. Hood & E. R. Priest 1981; T. Török & B. Kliem 2003). The resultant oscillations from this process are considered candidate mechanisms for QPPs (M. Gordovskyy et al. 2014; R. F. Pinto et al. 2016; J. A. McLaughlin et al. 2018; S. K. Mishra et al. 2023). The value of the critical twist depends on various factors, including aspect ratio, plasma and magnetic pressure ratios, and the structure of the surrounding magnetic field (A. W. Hood & E. R. Priest 1979; T. Török & B. Kliem 2003; M. R. Bareford, A. W. Hood & P. K. Browning 2013). Also significant is the loop's curvature, which can introduce new oscillation modes into the mechanism (P. J. Cargill, J. Chen & D. A. Garren 1994; T. van Doorsselaere, E. Verwichte & J. Terradas 2009) and affects the stability of the loop (M. R. Bareford et al. 2016).

Recently C. Smith, M. Gordovskyy & P. K. Browning (2022) demonstrated in a simulation of a kink-unstable coronal loop, coupled to a radiative transfer model of microwave emissions, that slowly decaying microwave oscillations were emitted from the reconnection site irrespective of the inclusion or exclusion of energetic electrons in their gyrosynchrotron (GS) radiation calculations. These oscillations, resembling QPPs, may result from a standing global MHD mode modulating the radiation emitted by the reconnecting plasma. While the precise mechanism driving these oscillations remains unidentified, 'structural oscillations' (i.e. sausage, kink, torsional modes, etc.) are potential candidates. It should be noted that C. Smith et al. (2022) also identify strong higher frequency QPPs associated with rapid variations in the electron acceleration process, possibly due to the triggering of anomalous resistivity. This is an example of the generation of QPPs by temporal (and spatial) variations in energetic electron acceleration, which may be a key mechanism for QPPs as found by G. D. Fleishman, T. S. Bastian & D. E. Gary (2008) and H. Collier et al. (2024). However, our focus here is on characterizing the MHD modes that arise in a reconnecting loop, as well as their potential observable signatures.

Motivated by these recent findings, we aim to explore the relationship between the structural oscillations of kink-unstable coronal loops and the observed oscillations in emitted GS radiation. To this end, we conduct MHD simulations of straight and curved twisted coronal loops undergoing the kink instability. We identify the oscillations of the loop and the internal plasma parameters resulting from this process and determine their connection with the emitted radiation. Since our main interest here is the MHD oscillations, we calculate only the emission from thermal plasma, which should be most strongly correlated with these oscillations. Emission from non-thermal electrons has been considered by C. Smith et al. (2022), but this has a more complex signature including high-frequency pulsations likely associated with time variations in the energy release and acceleration processes, which are outside the scope of this paper. We note that purely thermal flares are observed, albeit rarely (D. E. Gary & G. J. Hurford 1994; G. D. Fleishman, G. M. Nita & D. E. Gary 2015).

Section 2 describes the straight and curved loop models, their implementation within 3D resistive MHD simulations, and the methodologies used for identifying structural oscillations and calculating GS radiation. Results are presented in Section 3 and discussed in Section 4, focusing on the effect of curvature and the implications of these results for flares and QPPs.

2 METHODOLOGY

We investigate two models of a kink-unstable coronal loop in conditions representative of the solar corona, using MHD simulations described in Section 2.1. The first model, introduced in Section 2.2, represents a straight coronal loop within a constant-density environment. This simpler model serves as a basis for understanding the more realistic curved loop model, simulated in a gravitationally stratified atmosphere, discussed in Section 2.3. Section 2.4 explains how the GS radiation is calculated, while Section 2.5 focuses on the edge detection algorithm used for identifying sausage- and kink-mode oscillations.

Table 1. Normalization constants used in LARE simulations, including user-defined values (L_0, B_0, ρ_0) and their derived counterparts. Values used in the straight and curved loop mode simulations are listed.

Normalization constant	Definition	Value (straight loop)	Value (curved loop)
L_0	Loop-top radius	12×10^6 m	4×10^6 m
B_0	Loop-top magnetic field strength	0.02 T	0.02 T
ρ_0	Background coronal density	10^{-11} kg m^{-3}	3×10^{-11} kg m^{-3}
v_0	$B_0/\sqrt{\mu_0 \rho_0}$	5.64×10^6 m s^{-1}	3.26×10^6 m s^{-1}
P_0	B_0^2/μ_0	318 Pa	318 Pa
t_0	L_0/v_0	2.07 s	1.23 s
j_0	$B_0/(\mu_0 L_0)$	1.33×10^{-3} A m^{-2}	3.98×10^{-3} A m^{-2}
ϵ_0	v_0^2	3.18×10^{13} J kg^{-1}	1.06×10^{13} J kg^{-1}
T_0	$(1.2 m_{\mathrm{p}} \epsilon_0)/k_{\mathrm{B}}$	4.62×10^9 K	1.54×10^9 K
η_0	$\mu_0 L_0 v_0$	8.51×10^7 Ω m	1.64×10^7 Ω m

2.1 Solving the resistive MHD equations

We solve a form of the resistive 3D MHD equations in the Lagrangian regime, incorporating a viscous force term denoted as $\boldsymbol{f}_{\mathrm{visc}}$, which is implemented to capture weak shocks within the system (T. D. Arber et al. 2001). The equations can be expressed as follows:

$$\frac{D\rho}{Dt} + \rho \nabla \cdot \boldsymbol{v} = 0, \tag{1}$$

$$\rho \frac{D\boldsymbol{v}}{Dt} = (\nabla \times \boldsymbol{B}) \times \boldsymbol{B} - \nabla P + \boldsymbol{f}_{\mathrm{visc}}, \tag{2}$$

$$\frac{D\boldsymbol{B}}{Dt} = (\boldsymbol{B} \cdot \nabla)\, \boldsymbol{v} - \boldsymbol{B}\, (\nabla \cdot \boldsymbol{v}) - \eta \nabla \times (\nabla \times \boldsymbol{B}), \tag{3}$$

$$\frac{D\epsilon}{Dt} = -\frac{P}{\rho} (\nabla \cdot \boldsymbol{v}) + \frac{\eta}{\rho} j^2, \tag{4}$$

$$P = \rho \epsilon \, (\gamma - 1)\,. \tag{5}$$

Here, the mass density is denoted by ρ, plasma velocity by $\boldsymbol{v}$, magnetic field by $\boldsymbol{B}$, pressure by P, magnetic resistivity by η, specific energy density by ϵ, current density by j, and the heat capacity ratio, set to 5/3, by γ. While thermal conduction and radiation could influence the observational predictions of our model, they are not incorporated into this research as they were not initially considered by C. Smith et al. (2022), with whom we are comparing. Equations are expressed in dimensionless form, but the results are presented in dimensional form. The latter is necessary for calculating GS emissions. The normalization constants, which scale the straight and curved loop models, are defined in Table 1.

The viscous force term $\boldsymbol{f}_{\mathrm{visc}}$ incorporated in our simulations was initially developed by E. J. Caramana, M. J. Shashkov & P. P. Whalen (1998) and later adapted to be used in MHD by T. D. Arber et al. (2001). This term consists of three contributions. The first contribution involves approximating the fluid as a set of finite volume masses distributed across a staggered grid, following the method proposed by J. Von Neumann & R. D. Richtmyer (1950). The term is calculated by considering the non-linear energy exchange that arises from inelastic collisions among these particles. A second linear term is then included to mitigate non-physical oscillations that may occur behind shock fronts. This approach was first introduced by R. Landshoff (1955). Finally, a third term is included to account for errors arising from dividing a continuous fluid into finite volume masses. This correction is necessary to prevent inaccurate viscous dissipation calculations due to self-similar isentropic compression, as discussed by E. J. Caramana et al. (1998). E. J. Caramana et al. (1998) combined the work of R. B. Christensen (1990) and D. J. Benson & S. Schoenfeld (1993) to achieve this, introducing a term that deactivates the artificial viscosity in smooth regions of the flow. Combined, these three terms effectively capture weak shocks and contribute a value comparable to the kinetic energy density difference between a plasma element at a grid point and its nearest neighbours.

The resistive MHD equations are solved using LARE3D, a Lagrangian remap code, developed by T. D. Arber et al. (2001). We apply zero gradient boundary conditions (except for the velocity at $z = 0$) for the curved loop model (see Section 2.3). We utilize a current-driven anomalous resistivity, in which the resistivity (η) increases when the current density exceeds a critical value (j_{crit}):

$$\eta(j) = \begin{cases} 10^{-6}, \text{ if } j \leq j_{\mathrm{crit}}; \\ 10^{-3}, \text{ if } j \geq j_{\mathrm{crit}}. \end{cases} \tag{6}$$

The chosen value of j_{crit} is specific to each model and is defined in its respective sections.

2.2 Straight loop model

The development of the kink instability and subsequent reconnection in straight twisted loops has been studied extensively (P. K. Browning & R. A. M. Van der Linden 2003; P. Browning et al. 2008; M. R. Bareford et al. 2013; M. R. Bareford & A. W. Hood 2015; R. F. Pinto, N. Vilmer & A. S. Brun 2015; A. W. Hood et al. 2016; B. Snow et al. 2017; J. Reid et al. 2018). We construct a force-free straight twisted loop of length $L = 20$ following the model used in A. W. Hood, P. K. Browning & R. A. M. van der Linden (2009), which has previously found success in the study of MHD avalanches resulting from interacting kink-unstable coronal loops (K. V. Tam et al. 2015; A. W. Hood et al. 2016; J. Reid et al. 2018). The initial magnetic field for this model, in cylindrical coordinates, is a force-free equilibrium:

$$B_\theta = \begin{cases} \lambda r \left(1 - r^2\right)^3, & \text{if } r < 1; \\ 0, & \text{if } r \geq 1. \end{cases} \tag{7}$$

$$B_y = \begin{cases} \sqrt{1 - \frac{\lambda^2}{7} + \frac{\lambda^2}{7}\left(1 - r^2\right)^7 - \lambda^2 r^2 \left(1 - r^2\right)^6}, & \text{if } r < 1; \\ \sqrt{1 - \frac{\lambda^2}{7}}, & \text{if } r \geq 1. \end{cases} \tag{8}$$

Here, θ represents the azimuthal angle in the x–z plane, r denotes the radius from the origin in the x–z plane, and λ signifies the degree of twist in the flux rope. The flux rope undergoes the kink instability when $\lambda > \lambda_{\mathrm{c}}$, where λ_{c} stands for the critical twist. This parameter is also constrained by the requirement that B_y^2 must remain positive, limiting λ to be less than 2.438 (A. W. Hood et al. 2009). We select a value, $\lambda = 2.3$, just above the threshold for the ideal kink instability for a loop with a radius-to-length ratio of 0.05. For simplicity, we use a constant-density atmosphere instead of a stratified atmosphere, with ρ and ϵ set to 1.0 and 0.01, respectively. We select j_{crit} manually, examining the system before reconnection and selecting a value of j just above the equilibrium value. This value was set to $j_{\mathrm{crit}} = 5.0$.

We use a three-dimensional grid, bounded by [−3:3, −10:10, −3:3] with 321 × 641 × 321 grid points. The dimensions of this model are chosen to later match, as closely as possible, the resolution of the curved loop model. The ratio of the magnetic field at the centre of the flux rope to the background magnetic field is 2.0, while the plasma beta is 0.01 inside the loop and 0.05 outside the loop.

2.3 Curved loop model

More realistically, coronal loops are curved with their ends rooted in the photosphere, which may affect both their energy release and oscillations. Various models of curved and twisted coronal loops exist and have been previously used to study topics such as their interaction with non-uniform magnetic fields (F. Reale et al. 2016), factors influencing their critical twist (V. S. Titov & P. Démoulin 1999; T. Török, B. Kliem & V. S. Titov 2004; T. Török & B. Kliem 2005), and the release of energy in MHD avalanches (G. Cozzo et al. 2023). We use the model developed by M. Gordovskyy et al. (2014), which has previously been used by R. F. Pinto et al. (2016), M. Gordovskyy, P. K. Browning & E. P. Kontar (2017), and C. Smith et al. (2022) to study the observational signatures of thermal and non-thermal particles in kink-unstable coronal loops and by M. R. Bareford et al. (2016) to investigate the influence of field geometry and various thermodynamic effects on the stability of twisted flux tubes.

We begin by initializing an untwisted magnetic field by positioning two magnetic monopoles beneath the numerical domain, given by

$$\boldsymbol{B}(t=0) = B_1 \left(\frac{\boldsymbol{r}-\boldsymbol{m}_1}{|\boldsymbol{r}-\boldsymbol{m}_1|^3} - \frac{\boldsymbol{r}-\boldsymbol{m}_2}{|\boldsymbol{r}-\boldsymbol{m}_2|^3} \right). \tag{9}$$

Here $\boldsymbol{B}$ represents the magnetic field of the flux rope, B_1 scales the magnitude field strength of the loop, and $\boldsymbol{r}$ is the position vector from the origin. The vectors $\boldsymbol{m}_1$ and $\boldsymbol{m}_2$ indicate the positions of the two monopoles: $\boldsymbol{m}_1 = (0, a, -h)$ and $\boldsymbol{m}_2 = (0, -a, -h)$. The parameter a corresponds to the position of the footpoints on the photosphere. The depth of the monopoles beneath the domain is represented by h. We use the values $B_1 = 50$, $a = 6.4$, and $h = 3.2$.

The twist is created by applying slow vortical motions to each of the loop's circular footpoints. We utilize the method developed by M. R. Bareford et al. (2016), which injects twist similar to M. Gordovskyy et al. (2014) but at a consistent rate that prevents twist dissipation. The azimuthal velocity within each circular footpoint region is given by

$$v_{\mathrm{rot}}(r, t) = \psi(r)\zeta(t), \tag{10}$$

$$\psi(r) = r\left[1 - \tanh\left(\frac{r-R}{\chi}\right)\right], \tag{11}$$

$$\zeta(t) = \frac{w_{\mathrm{twist}}}{2} \tanh\left(\frac{t-t_1}{\tau_1}\right) \tanh\left(0.5 - \frac{t-t_2}{\tau_2}\right). \tag{12}$$

Equation (11) describes the spatial distribution of the twisting motions, where the r represents the radius measured from the centre of the footpoint, while R is the radius of the footpoint. The rotational velocity gradually increases from the centre of the footpoint towards its edge, declining sharply to zero near the footpoint edge. The position of the peak and the rate of decrease are dependent on the parameter χ. We have chosen $R = 0.5$ and $\chi = 0.05$, resulting in the rotational velocity peaking very close to $r = R$ and exhibiting a steep decline thereafter.

The temporal evolution of the azimuthal velocity is described by equation (12). Here, w_{twist} scales the magnitude of the rotational velocity. The parameters t_1 and τ_1 determine the onset time and the rate at which the twist increases, respectively. Similarly, t_2 and τ_2 determine the end time and the rate at which the twist decreases. The factor of 1/2 is included because the twisting profile is applied to both footpoints, which effectively doubles the rate of twist. We have chosen the following parameter values: $w_{\mathrm{twist}} = 0.02$, $t_1 = 120$, $t_2 = 460$, $\tau_1 = 40$, and $\tau_2 = 20$, selected to prevent significant dissipation, yet remain slow enough so that the field prior to instability onset is close to equilibrium. Once the loop becomes unstable, at a critical twist of about 4π, we switch off the rotational velocity. The described method of generating a twisted loop by injecting helicity at the footpoints can also be found in studies such as those performed by F. Reale et al. (2016), J. Reid et al. (2018), and G. Cozzo et al. (2023). It generates an approximate twisted force-free equilibrium for a curved loop; however, it should be noted that the initial twisting phase in these simulations is not intended to accurately represent the formation of a real twisted loop.

Using the aforementioned model, we construct an untwisted loop within a 512 × 512 × 512 Cartesian grid bounded by [$x = -10{:}10$, $y = -10{:}10$, and $z = 10{:}10$]. The initial configuration of the loop has a height of 8.34, a footpoint separation of 12.8, a length of 24, and a cross-section at the loop-top of 0.63 in dimensionless units. The magnetic field strength at the loop-top is evaluated to be 0.28, while the magnitude at the footpoint is determined as 4.82. Consequently, we observe an aspect ratio of 38.4 between the length of the loop and the cross-section at the loop-top, as well as a magnetic field strength ratio of 0.058 between the loop-top and the footpoints.

We construct a gravitationally stratified atmosphere, following M. Gordovskyy et al. (2014), with three layers: a chromospheric layer situated at the lower boundary of the domain, a transitional layer, and a coronal layer occupying the majority of the domain. The density profile is given by

$$\rho(z) = \rho_1\,\mathrm{e}^{-\frac{z-z_{\mathrm{c}}}{z_1}} + \rho_2\,\mathrm{e}^{-\frac{z-z_{\mathrm{c}}}{z_2}}. \tag{13}$$

Here, ρ_1 denotes the density of the chromosphere, ρ_2 corresponds to the density of the solar corona, z_{c} represents the height of the transitional layer, and z_1 and z_2 are the gradients of the density in the transitional layer and chromospheric layer, respectively. This is consistent with empirical models, such as those discussed by J. E. Vernazza, E. H. Avrett & R. Loeser (1981). We set $\rho_1 = 5.15 \times 10^7$, $\rho_2 = 3.03$, $z_{\mathrm{c}} = 4.675 \times 10^{-7}$, $z_1 = 5.5 \times 10^{-8}$, and $z_2 = 5.0 \times 10^{-6}$, with a factor of 10^4 difference between the density of the chromospheric and coronal layers. These parameters result in a temperature of $\sim 10^5$ K at the chromospheric level and $\sim 10^7$ K at the coronal level. The plasma beta starts at 0.1 at the footpoints, decreases to 0.005 in the lower corona, and rises to 0.01 at the loop-top.

To determine the critical current, we adopt the criterion employed by M. Gordovskyy et al. (2014), assuming plasma instabilities leading to increased resistivity arise when the electron drift velocity surpasses the sound speed, i.e. $v_{\mathrm{drift}} > v_{\mathrm{thermal}}$. Consequently, the critical current is expressed as

$$j_{\mathrm{crit}}(\boldsymbol{r}) = \frac{2e}{m_{\mathrm{p}}}\sqrt{\gamma(\gamma-1)\rho(\boldsymbol{r})\sqrt{\epsilon(\boldsymbol{r})}}. \tag{14}$$

Here, $\boldsymbol{r}$ denotes the position vector, e represents the charge of an electron, and m_{p} is the mass of a proton. However, as discussed by M. Gordovskyy et al. (2014), it is crucial to consider that the current density in global MHD models is limited by the grid resolution. To address this limitation, we multiply the above equation by a factor of

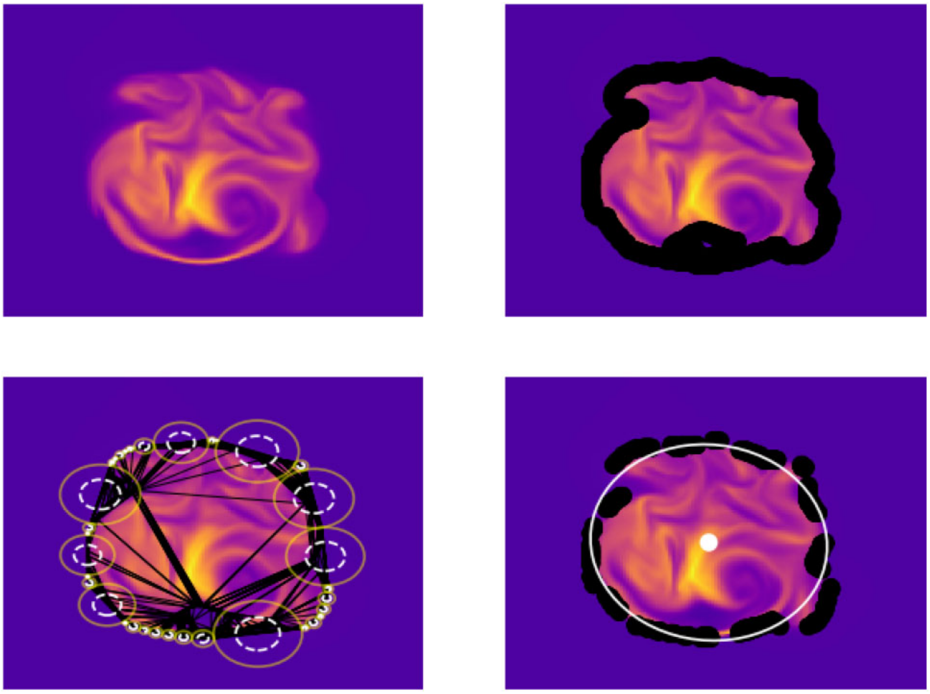

Figure 1. Demonstration of the edge detection algorithm in action. The top-left image shows an unprocessed input image (a 2D slice of pressure at the loop-top within the mid-plane of an evolving straight loop), while the top-right image displays the input image with outer edges detected (along with some inner edge artefacts). The bottom-left image illustrates Delaunay triangulation, with triangles plotted between each point in the edge data set. The solid circles depict the circumcircles of the edge points associated with the convex hull, and the dashed circles outline the alpha shape of these circumcircles. The bottom-right image exclusively features the outer edge points and a fitted ellipse.

$\delta L/R_\mathrm{L}$, where δL denotes the grid resolution and R_L is the Larmor radius of a proton. In dimensionless units, the critical current is

$$j_\mathrm{crit} = \frac{2eN}{m_\mathrm{p}}\sqrt{\gamma(\gamma-1)\mu_0\rho_0}, \tag{15}$$

where N is the number of grid points, typically in the direction with the lowest resolution.

2.4 GS radiative transfer code

Mildly relativistic electrons within a coronal loop gyrate in magnetic fields, leading to GS radiation emission. In a solar flare, this is typically in the microwave frequency range. However, accurately calculating GS radiation is computationally expensive. To overcome this, we use a fast GS radiative transfer code developed by G. D. Fleishman & A. A. Kuznetsov (2010), G. M. Nita et al. (2015), and A. A. Kuznetsov & G. D. Fleishman (2021).

The GS code enables the user to take the number density (cm^{-3}), temperature (K), and magnetic field (T) along a line of sight and calculate the GS radiation intensity (in solar flux units) emitted along that line of sight for a range of selected frequencies. It reduces the computational time required for calculating GS radiation by several orders of magnitude, yielding results within 1–10 per cent of their exact solutions. The algorithm has previously been implemented in the study of solar flares (M. Gordovskyy et al. 2017; E. P. Kontar et al. 2017; B. Chen et al. 2020), for investigating QPPs (G. Mossessian & G. D. Fleishman 2012; A. Altyntsev et al. 2016; E. G. Kupriyanova, T. I. Kaltman & A. A. Kuznetsov 2022; C. Smith et al. 2022; T. I. Kaltman & E. G. Kupriyanova 2023; M. Shi et al. 2023), and has found applications outside of solar physics (C. O. G. Waterfall et al. 2019; J. B. Climent et al. 2022).

We do not consider non-thermal electrons, which has been done by C. Smith et al. (2022). Instead, we use a thermal energy distribution and an isotropic pitch-angle distribution and compute the radiation emitted along multiple line of sights for both models. This focuses on oscillations associated with the MHD behaviour of the loop and allows us to determine how the emitted radiation evolves and identify periods of any fluctuating components that may be correlated with structural or parameter oscillations within the reconnecting loop, increasing our understanding of what mechanisms drive QPPs.

2.5 Structural oscillation analysis

We detect structural oscillations (oscillations of the loop structure, such as sausage modes, kink modes, etc.) by introducing a new method to isolate structures within a background plasma. Specifically, we isolate the loop-top of both models and study the MHD oscillations occurring therein. To achieve this, we construct a multistage algorithm that utilizes Canny edge detection (J. Canny 1986), Delaunay triangulation, and the construction of alpha shapes to determine the boundaries of structures in a 2D colour map. Sausage-mode and kink-mode oscillations can then be detected by fitting ellipses to the edges of the structure and tracking their evolution over time. A visual demonstration of this algorithm is provided in Fig. 1. This algorithm is not limited to identifying structural oscillations and may lend itself to additional potential applications.

The first step in this algorithm is to calculate the edges within a selected 2D slice. We focus on oscillations at the loop-top, so we take a 2D slice of the loop's mid-plane, corresponding to a parameter with a well-defined boundary between the inside and outside of the loop, in this case, pressure. We then remove all values within the image

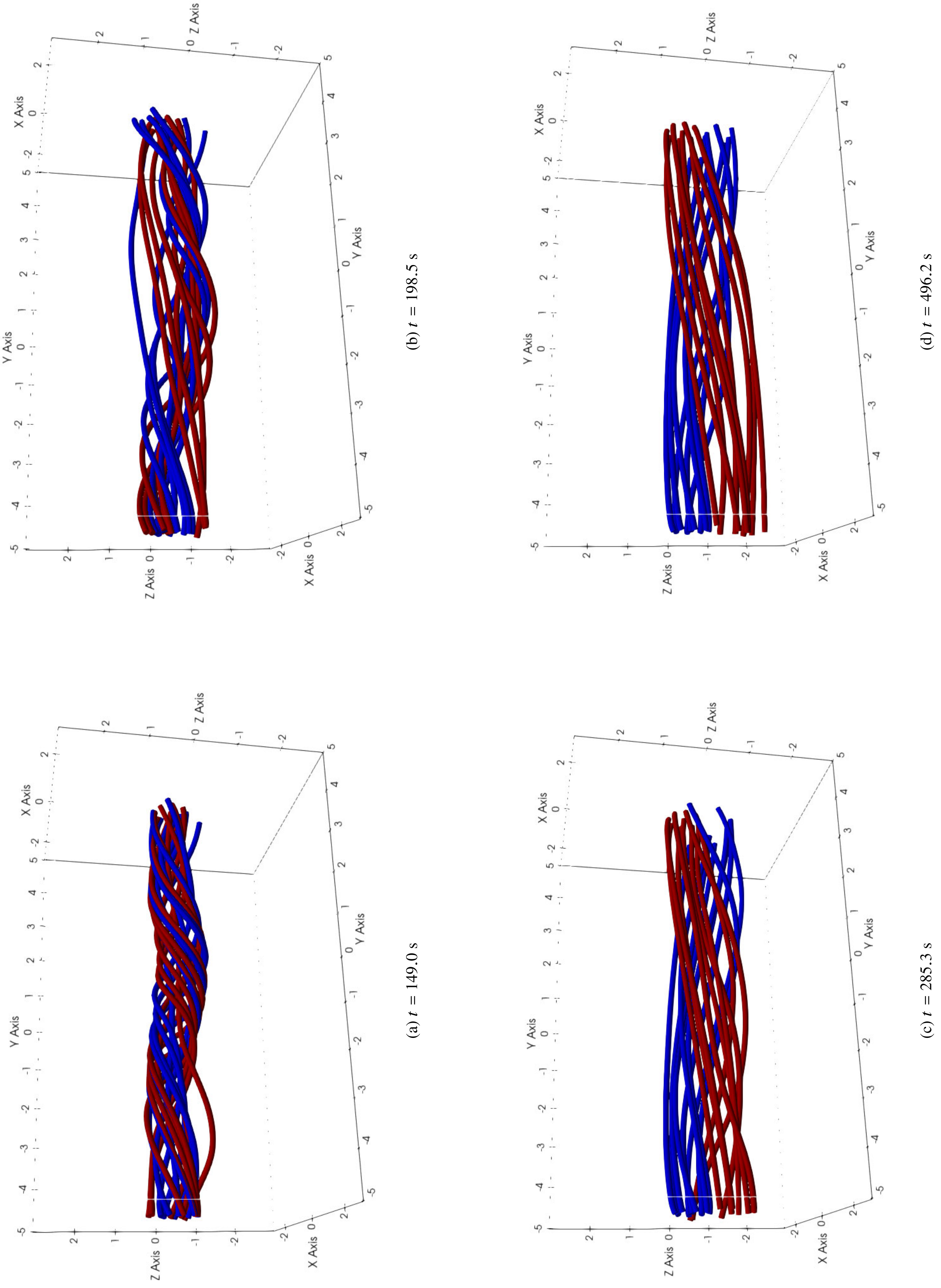

(a) t = 149.0 s

(b) t = 198.5 s

(c) t = 285.3 s

(d) t = 496.2 s

Figure 2. The evolution of the straight loop's interior magnetic field lines. The blue field lines originate from the footpoint at $y = -10.0$, while the red field lines originate from the footpoint at $y = 10.0$.

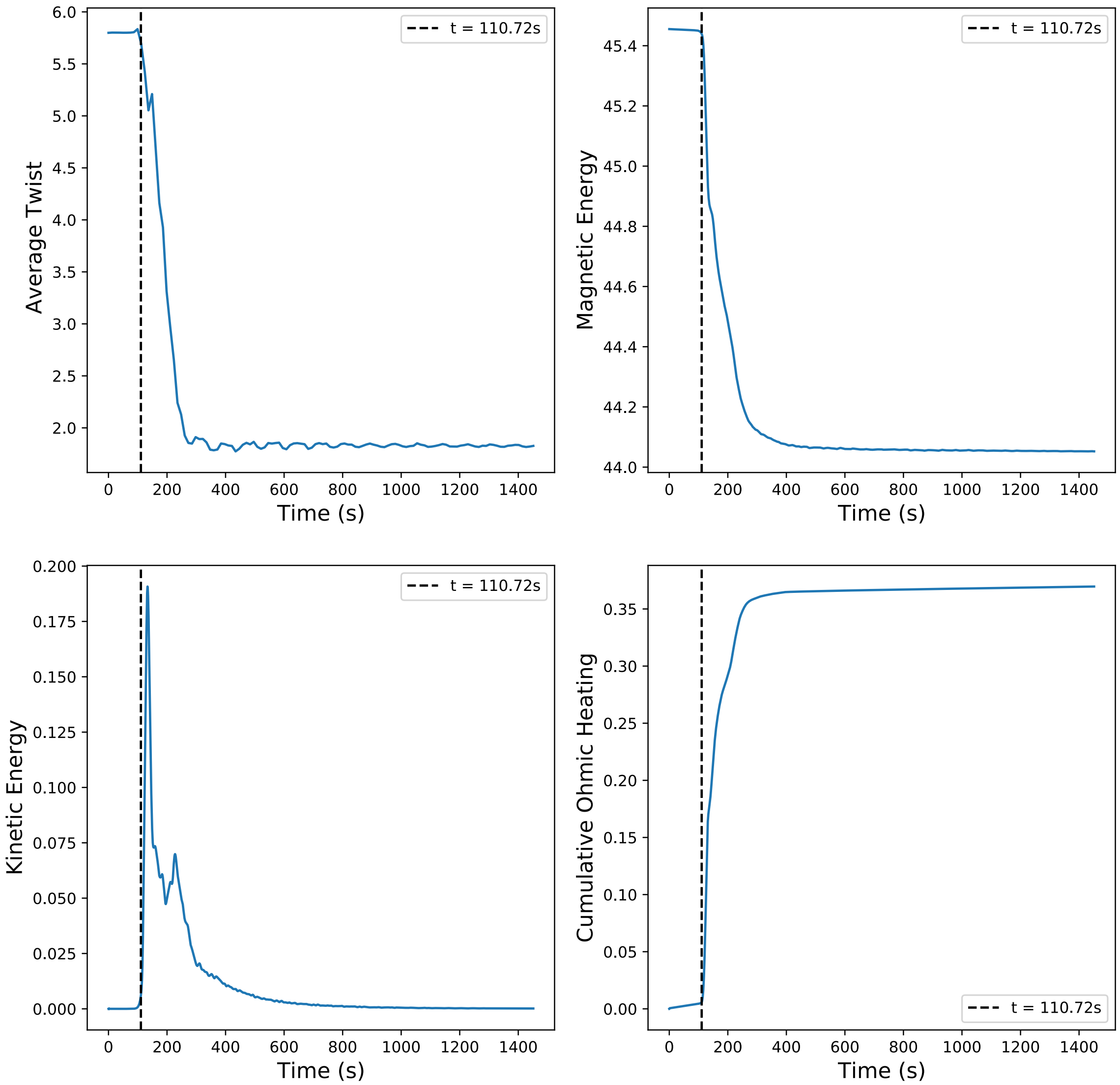

Figure 3. The temporal evolution of the average twist (top-left), total magnetic energy (top-right), kinetic energy (bottom-left) of the system, and cumulative Ohmic heating (bottom-right) for the straight loop. A black dashed line has been marked on each graph at the time at which the total magnetic energy starts to drop, differentiating between different phases of the loop's evolution.

below a threshold value. This results in a crude extraction of the loop-top from the background plasma, which we will further refine. From there, we implement the Canny edge detection algorithm to calculate the edges within the 2D image. The Canny edge detection algorithm (J. Canny 1986) has been applied to a variety of non-astrophysical scenarios (S. Agaian, A. Almuntashri & A. Papagiannakis 2009; X. Hou et al. 2009), and has seen continued development in the field of computer vision (W. Rong et al. 2014). In this paper, we use a traditional method outlined in E. Trucco & A. Verri (1998).

The Canny edge detection algorithm works as follows: first, we apply a grey scale transformation to the image and then blur it with a Gaussian kernel. This step helps minimize noise within the image. Subsequently, the edges of the image are identified by calculating the gradient of the image. This generates regions with sharp gradients (‘strong edges’) over a limited number of pixels and larger regions with more gradually changing gradients (‘weak edges’). Our final image should have clearly defined edges, so the next step is to convert weak edges into strong edges using non-maximum suppression. This technique involves evaluating for each pixel whether its gradient serves as the local maximum within a neighbourhood of pixels sharing the same gradient direction. If this criterion is met, the local maximum is retained along with any immediately adjacent weak edges, thereby forming a strong edge and enhancing the image's clarity.

The outcome is an image containing the extracted edges of the loop-top, with some inner edges left over that we wish to remove to accurately calculate the structural oscillations of the loop. We build upon the Canny edge detection algorithm by incorporating Delaunay triangulation and implementing alpha shapes to achieve this. We start by constructing a concave hull around the boundary edges of the isolated structure. To achieve this, we use Delaunay triangulation to generate a set of non-overlapping triangles from the edge data set. Subsequently, a convex hull is computed around these triangles, providing a preliminary estimate of the boundary between the loop-top and any remaining plasma that had not been removed earlier in the algorithm.

Then, we enhance the accuracy of the hull using alpha shapes. For each point along the convex hull, we compute a circumcircle

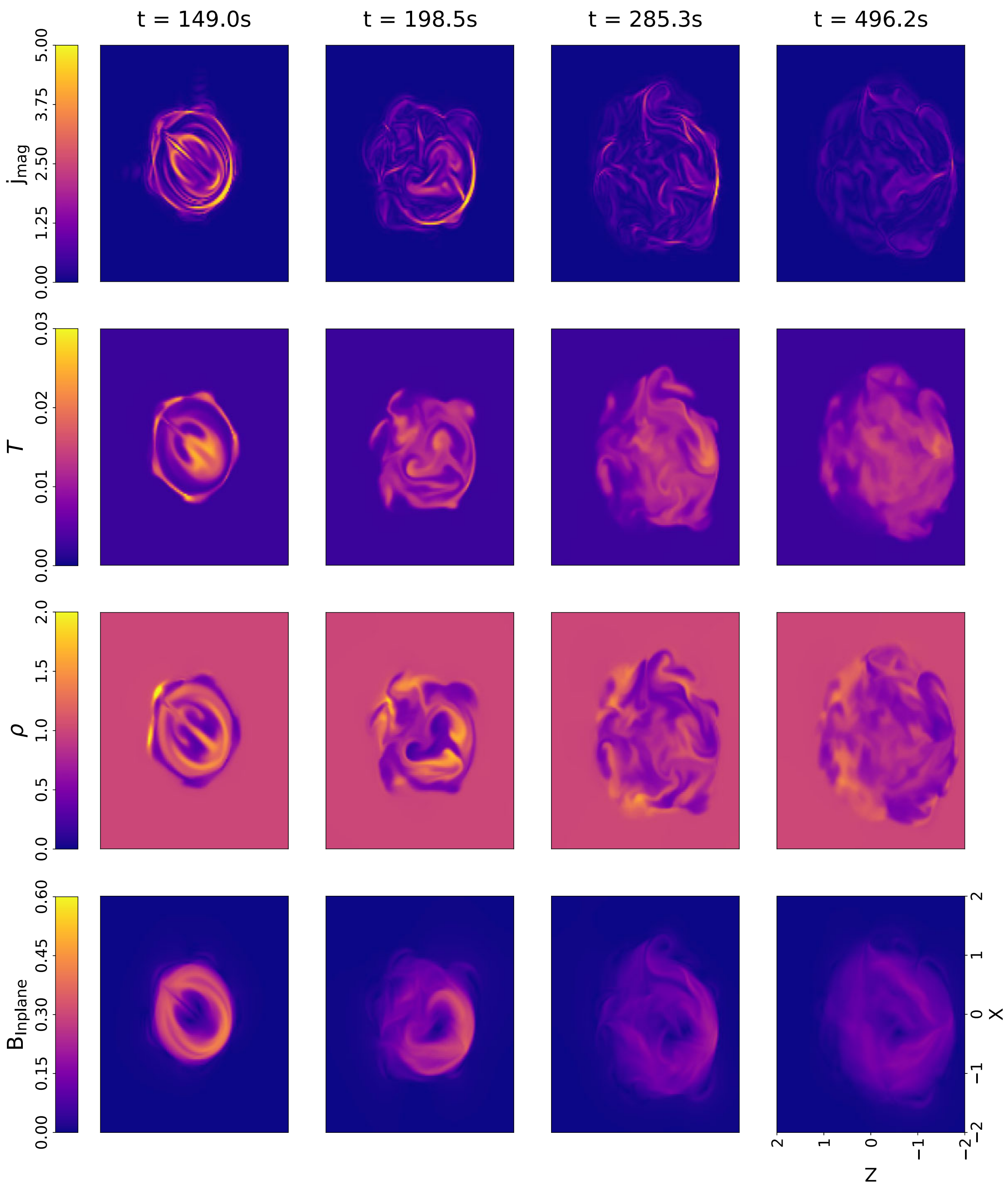

Figure 4. Colour maps illustrating the evolution of the in-plane magnetic field, density, and temperature of the straight loop in the X–Z plane at the mid-plane of the loop ($y = 0$) over time.

around the associated triangle's vertices. The circle's radius is then scaled by a parameter, α, resulting in the creation of an alpha shape. Points within the edge data set that fall within this alpha shape are designated as 'boundary edges', and are separated from the interior edges. To create an accurate hull around the loop-top, the α parameter must be carefully chosen. A larger α value produces a less-detailed convex boundary, whereas a smaller value risks missing potential points along the boundary. In our analysis, we opted for $\alpha = 0.5$ for the straight and curved loop.

The structure is now isolated from the background plasma and can be used for other purposes if desired. To identify structural oscillations, we fit an ellipse to the isolated loop-top for each time-step. By tracking the evolution of the fitted ellipse, we can isolate kink-mode oscillations (through the motion of the elliptical centre) and sausage-mode oscillations (through changes in the area of the ellipse) in the reconnecting loop.

3 RESULTS

The kink instability was induced and simulated for both straight and curved loops. The resulting evolution, including magnetic reconnection, plasma heating, emitted radiation, and structural oscillations, is described below.

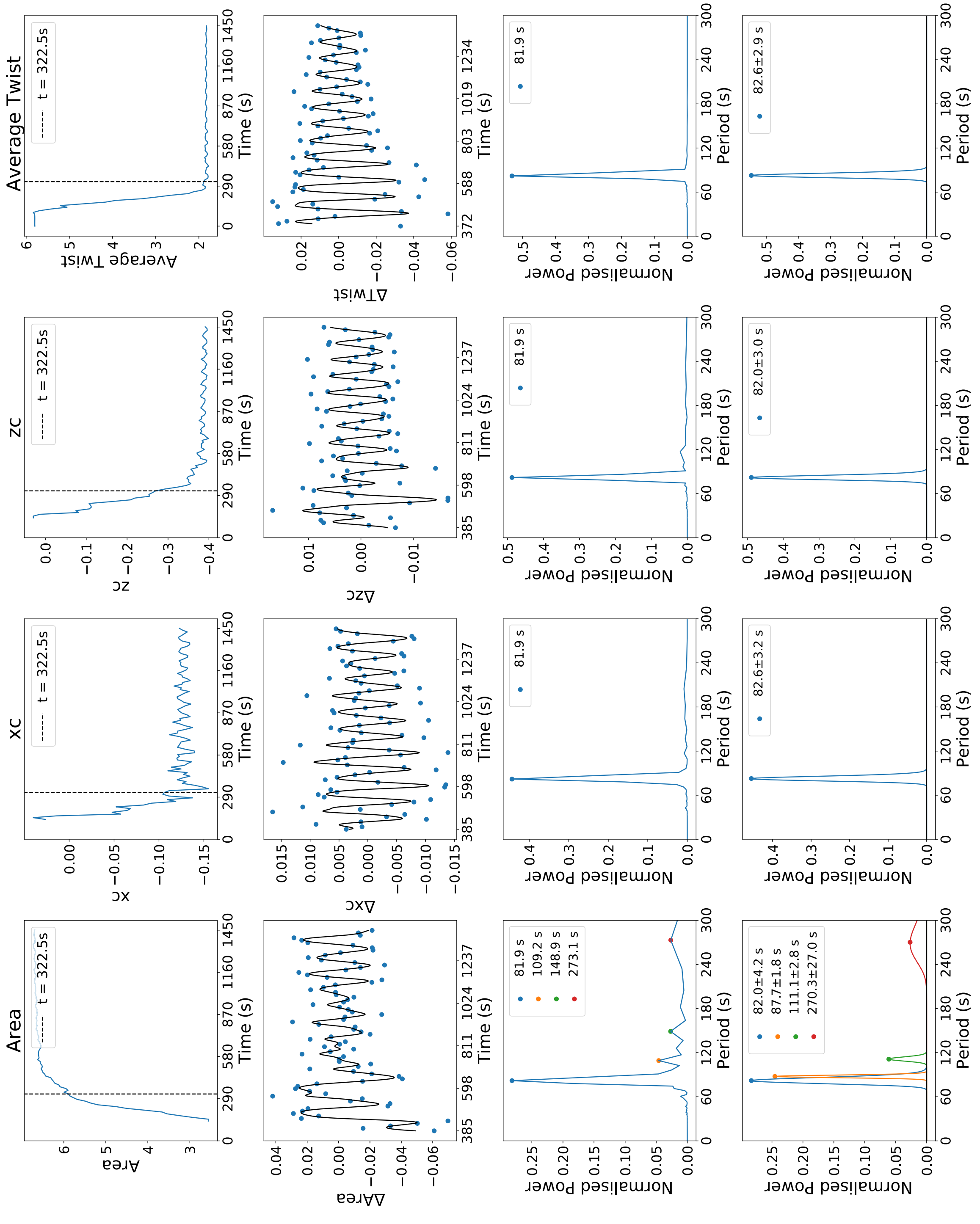

Figure 5. Analysis of the structural oscillations observed in the straight loop model. The first row illustrates how the fitted ellipses cross-sectional area, central coordinates (x_c and z_c), and how the average twist of the loop evolves over time. A dashed black line separates data points before and after 322.5 s. In the second row, the post 322.5 s data, with the removal of its moving average, are presented. The third row showcases the periods of the power spectrum of this processed data. Finally, the fourth row maps Gaussian peaks to the corresponding peak periods identified in power spectra.

3.1 Evolution of the straight loop

We generate a model of a straight coronal loop in a state of unstable force-free equilibrium, with a twisting parameter $\lambda = 2.3$ as described in Section 2.2. Upon starting the simulation, the loop undergoes the kink instability and begins to reconnect, eventually relaxing to a new equilibrium state.

Fig. 2 shows how the interior magnetic field lines develop as the system evolves. Fig. 3 depicts the evolution of both the average twist and the energetics of the system over time. We calculated the average twist by determining the total twist of 200 magnetic field lines distributed inside the loop around the central loop axis and then averaging these values. Additional visualization is provided in Fig. 4,

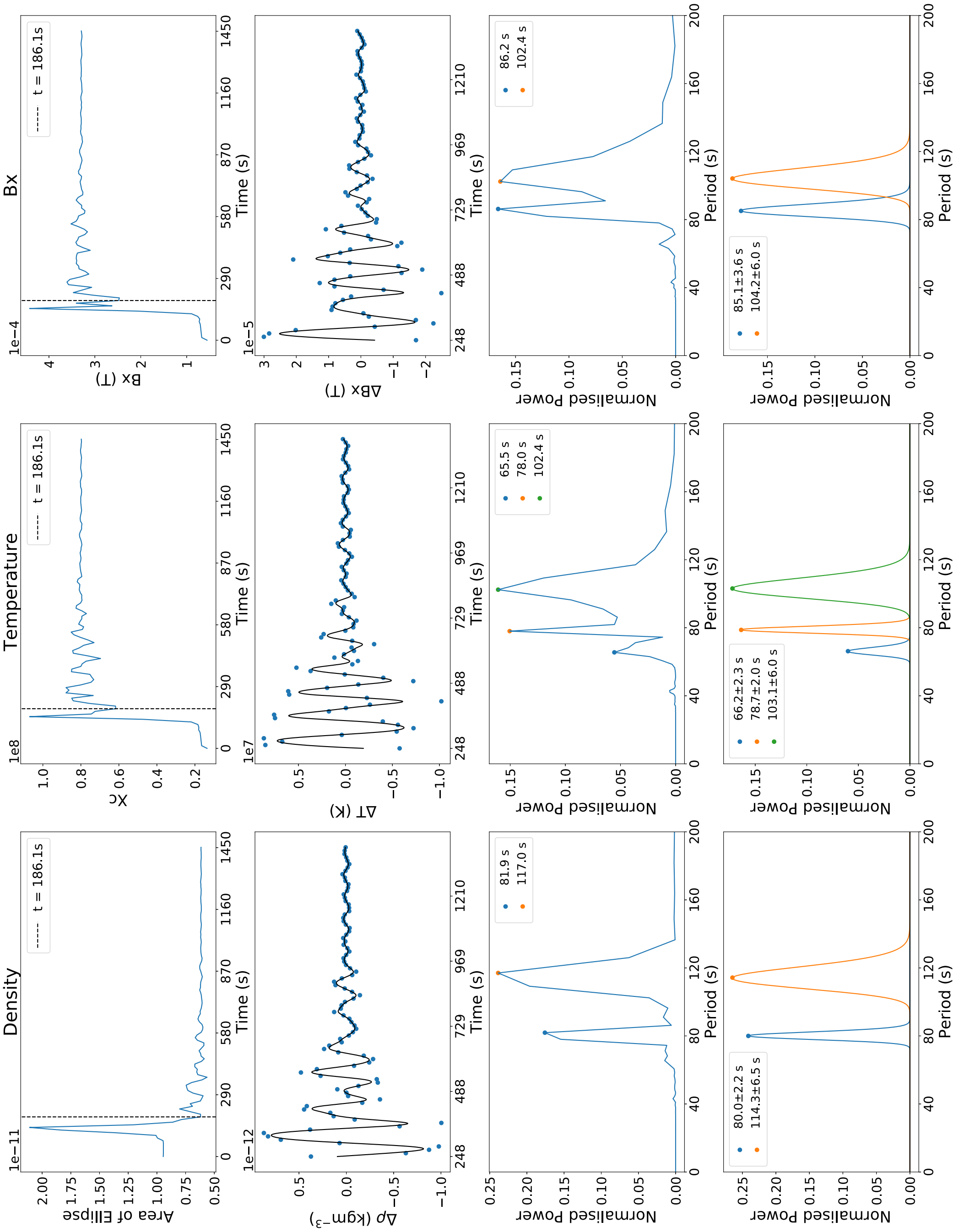

Figure 6. Analysis of parameter oscillations at the centre of the loop. The first column analyses the system's density, the second column examines temperature, and the third column, B_x. The rows follow the same structure as those in Fig. 5.

which takes a slice of the loop in the X–Z plane at $y = 0$, and shows how the in-plane magnetic field, density, temperature, and current magnitude within the loop change with time.

The simulation was run for 702 Alfvén times (1453 s). Between $t = 0$ s and around $t = 286$ s, inhomogeneities in the in-plane magnetic field, density, temperature, and current magnitude form as the kink instability progresses from its linear phase into its non-linear phase. Reconnection at multiple current sheets within the loop follows, and we observe similar magnetic field and energetic evolution to A. W. Hood et al. (2009). After around $t = 286$ s, the loop relaxes towards a new equilibrium with reduced twist and magnetic energy; however, we do not extend the simulation to reach a fully static equilibrium.

Post-reconnection, we observe multiple structural oscillations in the loop (Fig. 5). We take a cross-sectional slice of the loop (at the mid-plane $y = 0$) and use our edge-detection and ellipse-fitting algorithm to monitor the changes in the area and central coordinates (x_c and z_c) of the loop-top over time (see Section 2.5). We observe an expansion of the loop-top, likely driven by Ohmic heating that increases the loop's internal temperature and by reconnection of the loop's field lines with ambient untwisted field lines (M. Gordovskyy et al. 2014). We also observe lateral shifts in the loop-top in the x and z

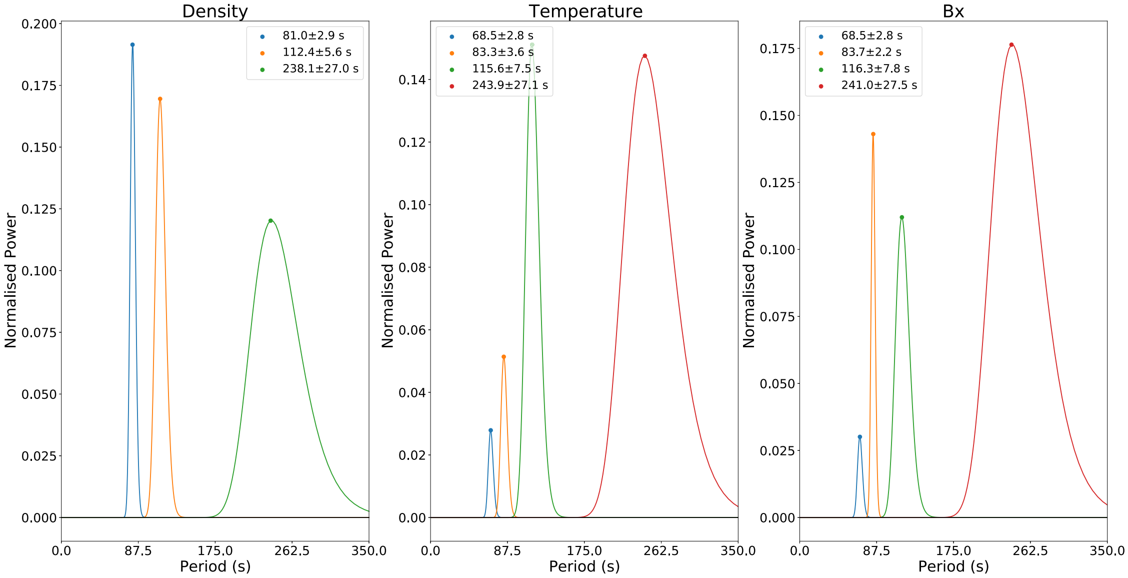

Figure 7. Periods of the power spectrum for internal parameter oscillations observed at $x = 0.5$, $z = 0.0$for the straight loop. The first column analyses the system's density, the second column examines temperature, and the third column, B_x.

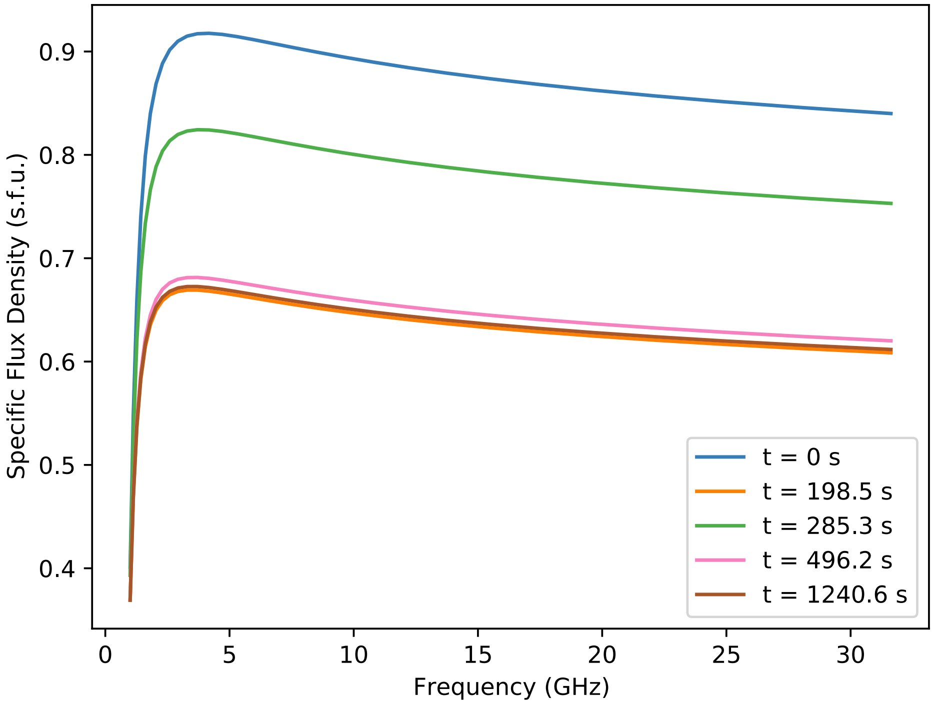

Figure 8. Intensity of GS radiation emitted from the loop-top as a function of frequency at various points in time (s) throughout the straight loop's evolution.

directions. The central coordinates oscillate around new equilibrium values mainly after about $t = 323$ s (though some oscillations are observed before this point). The expansion and the contraction of the cross-sectional area resemble a sausage-mode oscillation, and the swaying motions detected in x_c and z_c resemble a kink-mode oscillation. We also detect clear post-reconnection oscillations in the loop's average twist (see first panel of Fig. 3).

We analyse these structural oscillations further by removing a moving average from the original data and calculating the oscillations' power spectra. The periods contained within the spectra are then identified. For each oscillation, we observe multiple broad peaks that can be used to determine the dominant periods contributing to each oscillation (see lower panels of Fig. 5). Spectral leakage and inaccuracies are expected when calculating these periods due to limitations in the simulation's total length and temporal resolution. To address this, Gaussian peaks were fitted to each peak. The means of these curves provide a value for peak periods, while the variances serve as errors that allow for comparison with peaks from other power spectra.

We detect in each variable a dominant period at ∼83 s, along with smaller contributions detected in the sausage-mode oscillations. This common period suggests two things: the structural oscillations are

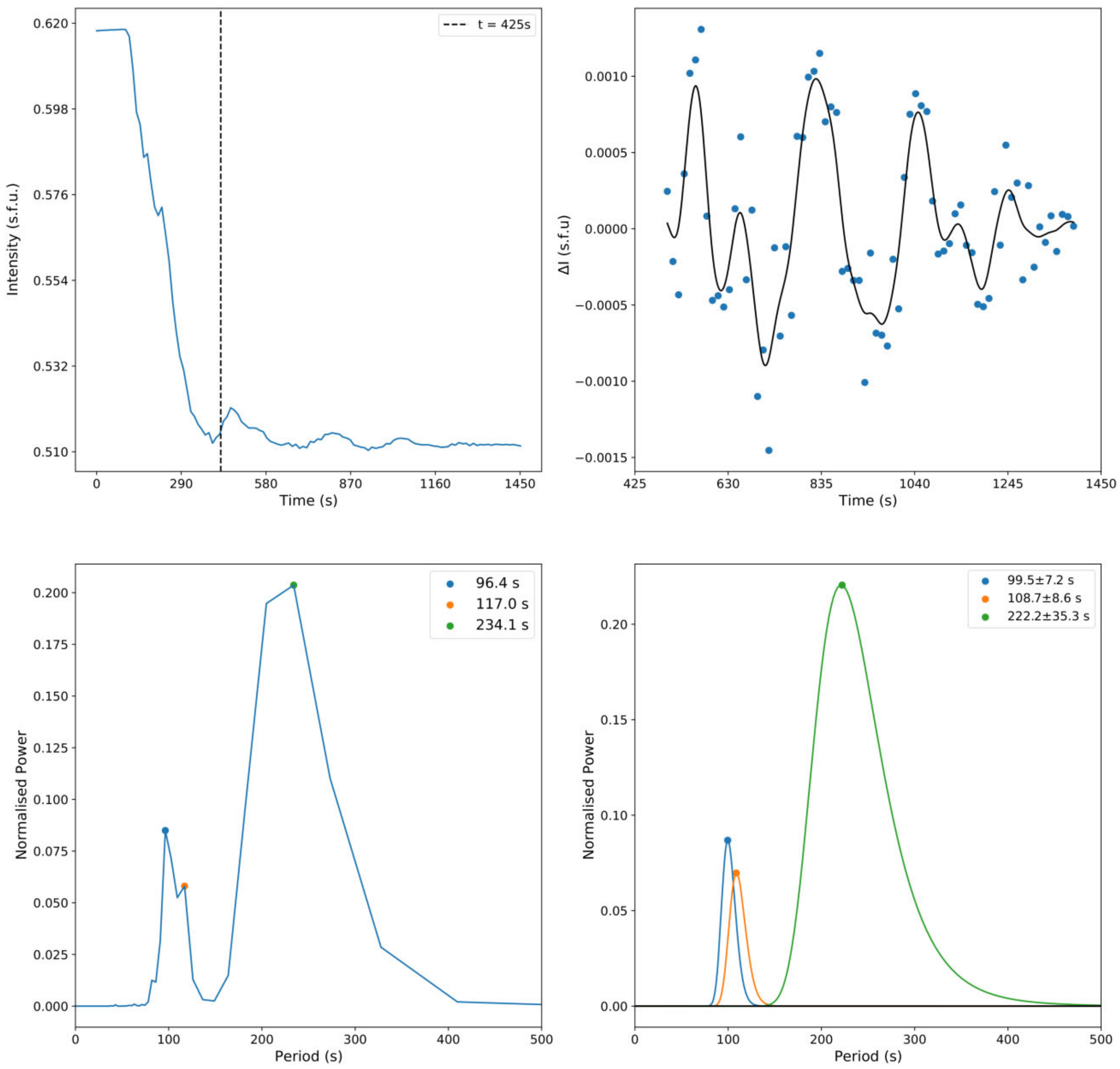

Figure 9. The variation of GS radiation at 1.2 GHz with time (top-left) for the straight loop, detrended GS radiation (top-right), the periods identified in its associated power spectrum (bottom-left), and Gaussian fits to those periods (bottom-right).

connected, and the oscillations observed in the average twist are likely due to the expansion and contraction of the loop rather than the presence of an additional 'torsional-like' Alfvén wave, which would be characterized by oscillatory rotational motions around the loop-top.

Using a similar methodology, we construct power spectra of oscillations detected in the density, temperature, and line-of-sight magnetic field (B_x) at the centre of the loop-top [0, 0, 0] (Fig. 6). These variables, in a complex and non-linear way, together determine the emitted GS radiation. Two common periods are observed in each quantity. The first overlaps with the ∼83 s mode identified in the structural oscillations. The second, at ∼107 s, aligns with a minor peak observed in the cross-sectional area power spectra. This suggests that the parameter oscillations are primarily associated with the observed structural oscillations. The other minor peaks observed may be associated with harmonics or other modes of oscillations not identified in this paper.

Away from the reconnection site, additional oscillations are detected in the density, temperature, and line-of-sight magnetic field. Fig. 7 shows that at point $x = 0.5$, $z = 0.0$, a new oscillation at approximately ∼240 s emerges alongside the ∼83 and ∼107 s oscillations. Interference could be a potential reason why this additional mode does not appear at the centre of the reconnection site.

Oscillations at ∼83 and ∼107 s are observed along with a new oscillation at ∼240 s at $x = 0.5$, $z = 0.0$. All three align with oscillations detected in the sausage mode.

Finally, we identify oscillations in the GS radiation emitted from the loop-top (see Section 2.4). To calculate the emitted radiation, we take ∼9000 lines of sight transverse to the loop, in the x-direction, near the mid-plane, equally spaced within a region bound by [−2:2, −0.67:0.67, −2:2], and record the density, temperature, and line-of-sight magnetic field along those lines. Subsequently, we partition this region into 356 subregions, and for each subregion, we average

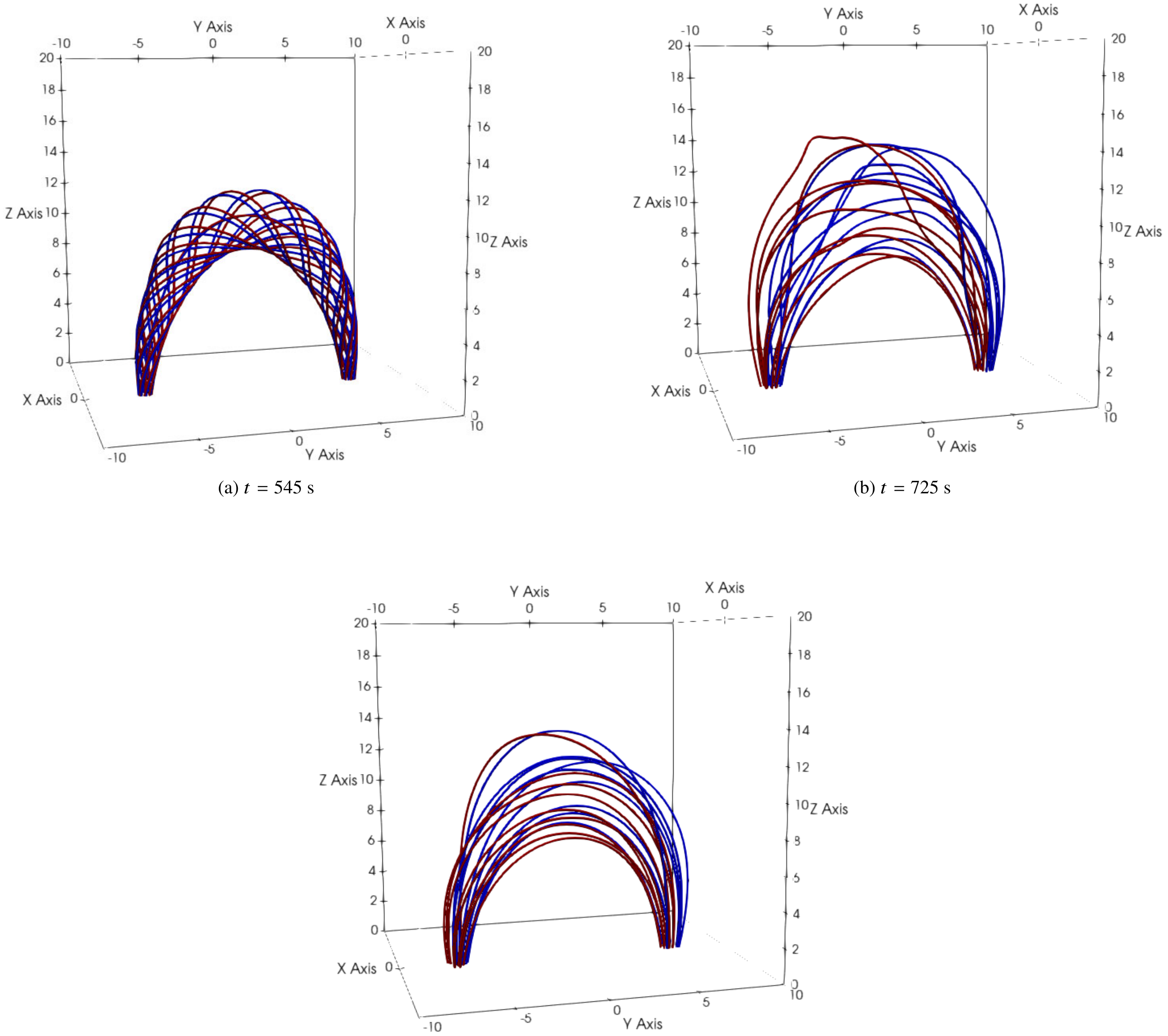

(a) $t = 545$ s

(b) $t = 725$ s

(c) $t = 1035$ s

Figure 10. Evolution of the curved model coronal loop's magnetic field lines in the *Y*–*Z* plane over time. The blue field lines originate from the footpoint at $y = -6.4$, while the red field lines originate from the footpoint at $y = 6.4$.

the aforementioned parameters for each point between each line of sight to reduce the computational expense of the GS calculations. We avoid taking an average of the whole loop-top as different segments of the loop contribute different quantities of GS radiation due to varying internal parameters throughout the simulation. We carefully select a number of subregions that strike a balance between reducing computational strain and ensuring that the final radiation calculated remains representative of the behaviour of the loop.

The GS microwave frequency spectra emitted from this region at different points in time are illustrated in Fig. 8. Continuous emission is predominantly observed around 1 GHz, with the total intensity decreasing over time as the magnetic field strength of the loop weakens. The spectra show typical shapes, with optically thick radiation at low frequencies rising to a peak, with a gradual decrease of intensity through the higher (optically thin) frequency range. We also detect oscillations across the calculated spectrum, similar to C. Smith et al. (2022). In Fig. 9, we focus on the radiation emitted at 1.2 GHz, noting that other frequencies exhibit similar behaviour. This choice of frequency for analysis means we are in the partially optically thick regime. This means the microwave emission may have a less direct correspondence with the underlying plasma and magnetic field parameters than in the optically thin regime.

A primary peak is observed at ∼222 s, with two secondary peaks around 107 s. These peaks align with those found in the internal parameter oscillations and also appear as minor peaks in the sausage-mode oscillations. Notably, no peak is observed at ∼83 s.

There is a complex relationship between the sausage-mode oscillations, internal parameter oscillations, and oscillations in the emitted GS radiation. This complexity is expected due to the highly non-linear mechanisms by which GS emission arises from plasma parameters and the magnetic field (G. Mossessian & G. D. Fleishman 2012; E. G. Kupriyanova et al. 2022; T. I. Kaltman & E. G. Kupriyanova

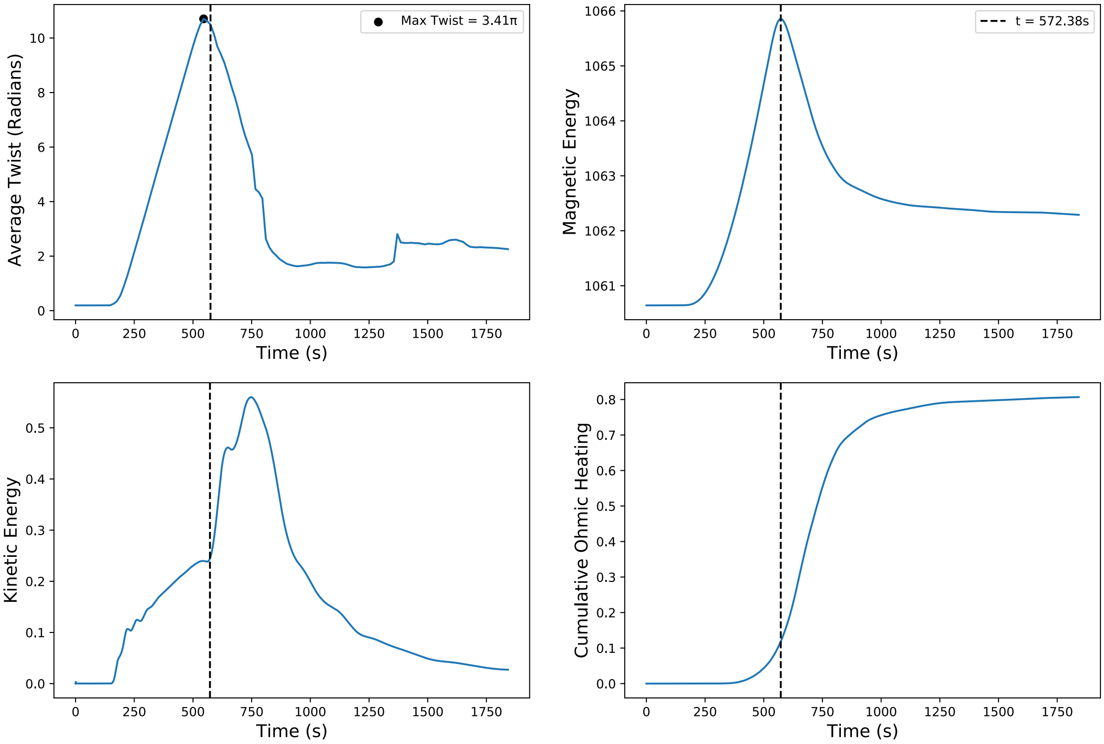

Figure 11. The temporal evolution of: average twist of the loop (top-left), total magnetic energy (top-right) and kinetic energy (bottom-left) of the system, and cumulative Ohmic heating (bottom-right). A black dashed line has been used to separate the initial setting up of the initial state and the resultant evolution.

2023). A notable feature is that though the 222.2 s mode is dominant in the emitted GS radiation and internal parameter oscillations (away from the centre loop-top), it is less prominent in structural oscillations. There are several potential explanations for this.

One possibility is that the 222.2 ± 35.2 s GS oscillation results from interference between the 111.28 ± 2.8 s and 82.0 ± 4.2 s peaks seen in the sausage-mode oscillations. Alternatively, other wave modes – undetected by the edge detection algorithm – could contribute to the emission oscillations. A potential candidate is a longitudinal acoustic mode, whereas a torsional mode can be ruled out since the $\sim$222 s peak would also appear in the average twist oscillations, which were not observed. Furthermore, since the radiation we analyse is in the optically thick region of the spectrum, it will be determined by the plasma and magnetic field across the line of sight in a complex way, and not just depend on the local conditions at the emission site.

3.2 Evolution of the curved loop

Following M. Gordovskyy et al. (2014), we induce the kink instability in a curved loop by applying a twist to the loop's footpoints. We inject a total twist of approximately 4π before the loop becomes unstable, reconnects, and relaxes towards a new equilibrium state.

We analyse the curved loop in a similar way to the straight loop. The simulation was run for 1500 Alfvén times (1845 s). Once the loop reaches an average twist of 3.41π, at around $t = 565$ s, the loop becomes unstable, indicating that some of the injected twist dissipated during this initial phase. The evolution prior to this is only to establish an unstable equilibrium, and this time corresponds to $t = 0$ for the straight loop discussed above. When the loop begins to reconnect, it exhibits similar behaviour to the straight loop concerning energetics and internal dynamics (see Figs 3 and 4) and is similar to previous work with this model (M. Gordovskyy et al. 2014; M. R. Bareford et al. 2016; R. F. Pinto et al. 2016; C. Smith et al. 2022).

The evolution of the loop's interior magnetic field lines is depicted in Fig. 10, while Fig. 11 illustrates the evolution of the average twist and energetics over time. The internal dynamics of the loop evolve similarly to the straight loop (Fig. 4). Discussions of behaviour prior to approximately $t = 565$ s will be omitted, as this phase serves solely to set up an unstable twisted approximate equilibrium and the dynamics are non-physical.

We again use our edge-detection and ellipse-fitting algorithm on a cross-sectional slice of the loop at $y = 0$ to quantify changes in the loop-top's area and central coordinates (x_c and z_c) over time (see Fig. 12). We observe expansion and contraction of the loop, similar to the straight loop, and lateral displacement. The direction of the lateral shift differs in the curved loop. This is due to the straight loop's symmetry, which results in a random initial shift, whereas the curvature of the curved loop provides a preferred direction. In Fig. 12, we also identify post-reconnection oscillations in the loop's average twist.

A single common period of approximately 190 s is observed in all four structural parameters. Additionally, a second period of about 270 s is observed in all parameters except the average twist. This suggests, similar to the straight loop, that the sausage-mode and kink-mode oscillations are connected, and the sausage mode drives oscillations in the loop's twist. However, unlike the straight loop, a unique period is observed in the average twist oscillations ($\sim$119 s), indicating the presence of a potential alternative mechanism that is also affecting the loop's twist.

Further oscillations in the density, temperature, and line-of-sight magnetic field are observed inside the loop-top over time, measured at coordinates [0, 0, 12] (Fig. 13). This point is located internally

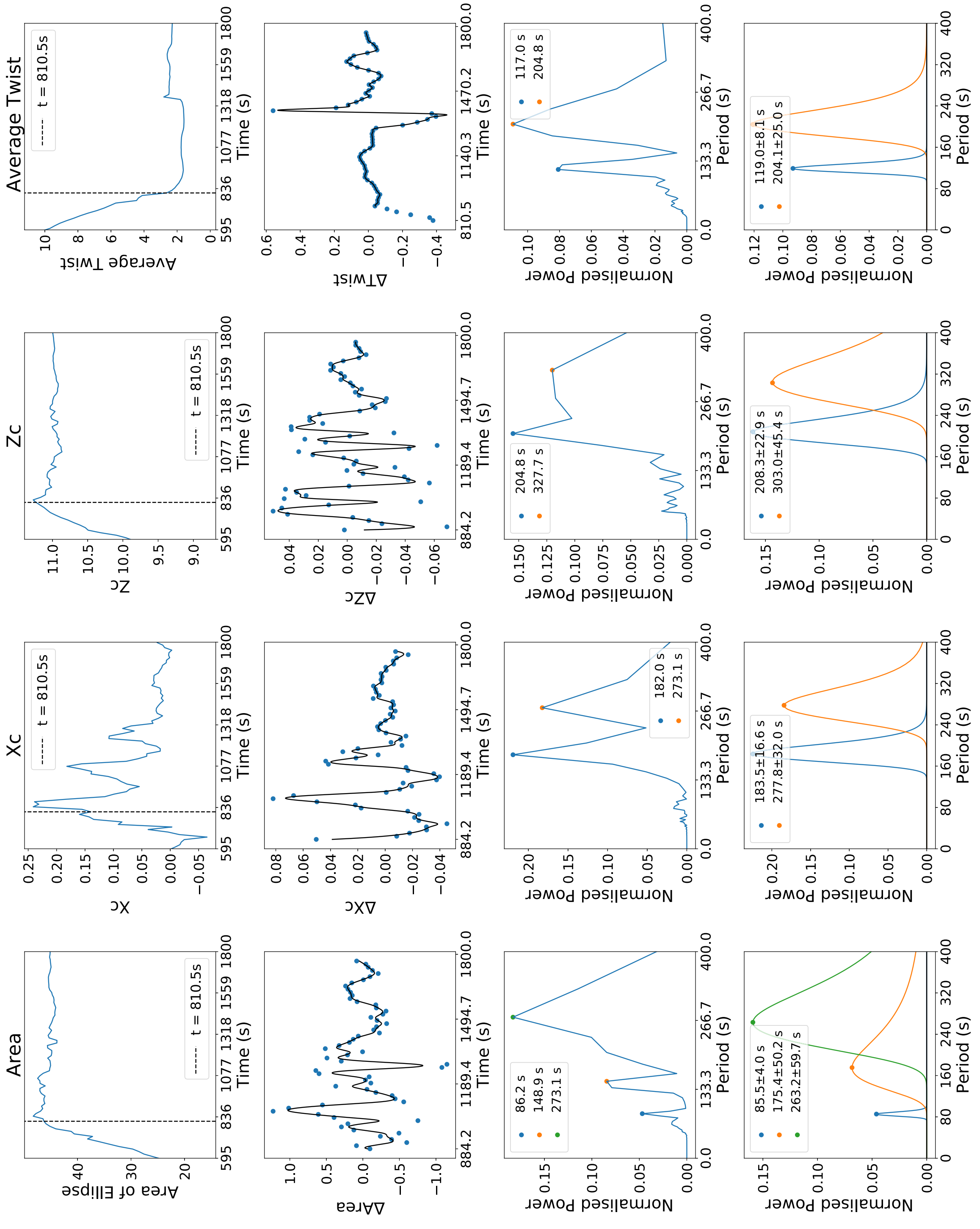

Figure 12. Analysis of the structural oscillations observed in the curved loop model, following the same structure as Fig. 5.

at the centre of the loop, drifts from the centre as the loop evolves, but remains within the loop-top throughout the simulation. A peak at ∼190 s is observed in the density and B_x oscillations, while a peak at ∼270 s is observed in all three variables. These two peaks are associated with the sausage-mode and kink-mode oscillations. A third peak at ∼119 s is also observed in all three variables. This peak aligns with the 119-s peak observed in the loop's average twist, suggesting that the internal parameters are also affected by the mechanism influencing the loop's average twist, perhaps torsional Alfvén waves.

To calculate the GS radiation, we use the same approach as the one used for the straight loop. However, this time we consider 18 350 lines of sight along the x-axis, bounded by [−10:10, −2:2, 7:14], divided into 356 subregions. Compared to the straight loop, we observe a wider range of emitted frequencies, resembling those seen in C. Smith et al. (2022).

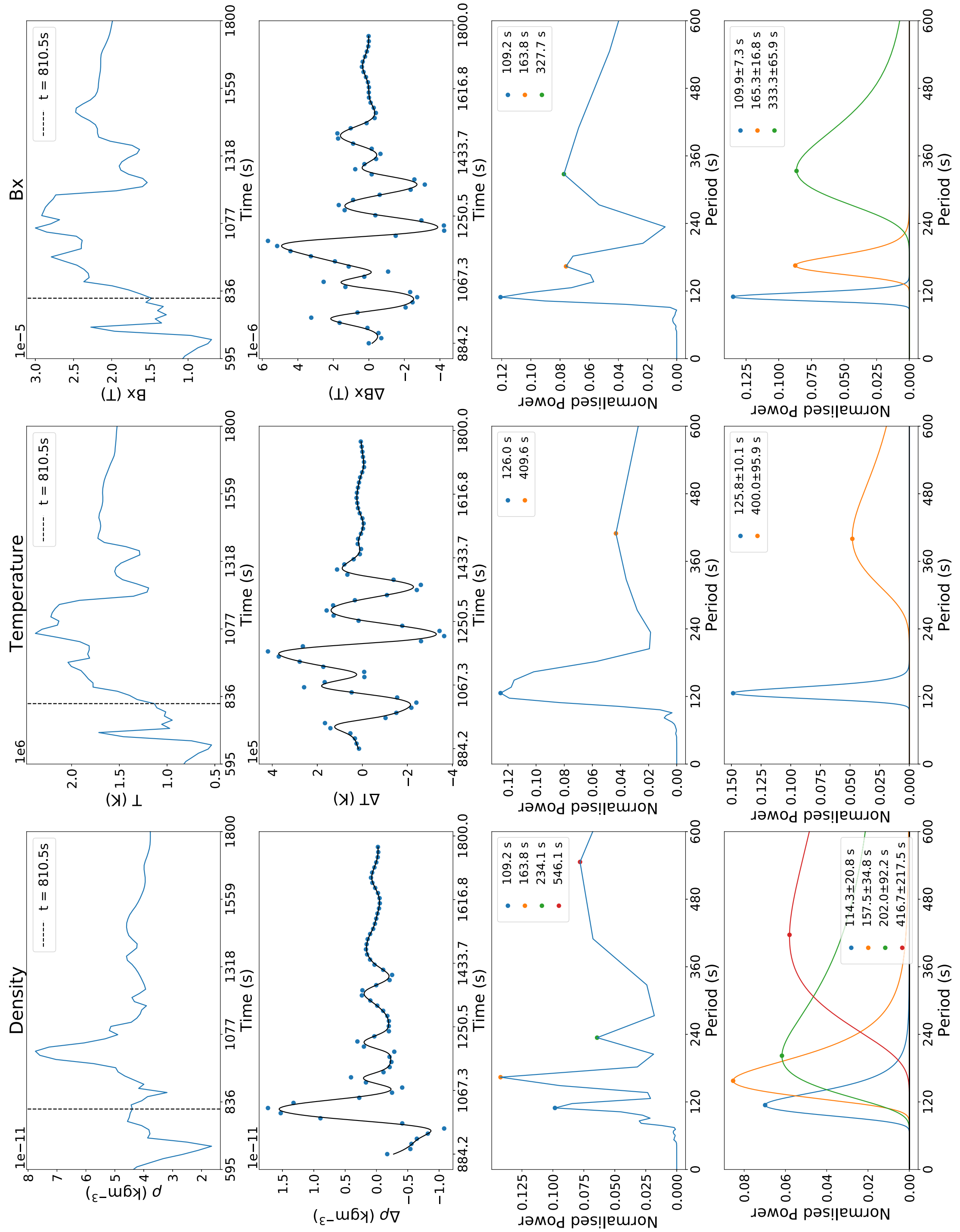

Figure 13. Analysis of parameter oscillations at [0, 0, 12], located at the mid-plane of the curved loop. The first column analyses the system's density, the second column examines temperature, and the third column, B_x. The rows follow the same structure as those in Fig. 6.

The intensity versus frequency distribution for the curved loop has the same shape as the straight loop (Fig. 7), with a peak at 15 GHz. Fig. 14 shows a map of GS radiation emitted from the coronal loop in the Y–Z plane at 15 GHz, at the same snapshots as in Fig. 10. A total of 146 800 lines of sight are grouped into 9025 averaged subregions, from which the emitted radiation is calculated. Brightenings and fine structure are observed within the loop. While this level of spatial resolution cannot be observed with current observational techniques, the figure provides insight into the origins of the emission peaks.

Fig. 15 focuses on oscillations at 15 GHz, noting that other frequencies exhibit similar behaviour. We observe two peaks: one at approximately 233 s and another around 526 s. The first peak aligns with the 270-s oscillations observed in the structural modes, suggesting that, similar to the straight loop, it is driven by sausage- and kink-mode oscillations.

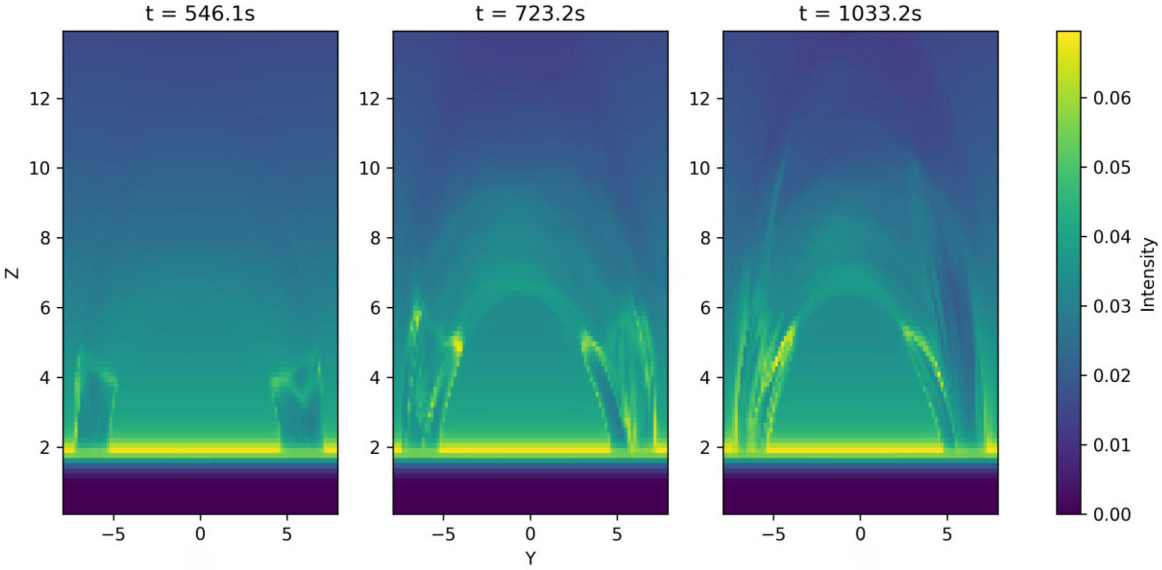

Figure 14. Normalized GS radiation at 15 GHz in the Y–Z plane (spanning $Y = -8$ to 8, $Z = 0$ to 14), for the same time-steps as images of the evolving curved coronal loop presented in Fig. 10.

However, the dominant peak at 526 s does not directly correspond to any structural oscillations. As in the straight loop, there is evidence to suggest that they may arise from interference effects. Interference of the peaks at 175.4 ± 50.2 and 263.2 ± 59.7 s area oscillations, 183.5 ± 16.6 and 277.8 ± 32.0 s in the x_c oscillations, and 208.3 ± 22.9 and 303.3 ± 45.4 s in the z_c oscillations gives a period similar to the 526-s peak. Additionally, interference between adjacent peaks in the density oscillations also aligns with the 526-s peak. We also note that the 119-s oscillation detected in the loop's average twist does not appear in the GS radiation oscillations. Though this mechanism remains unidentified, it does not significantly influence the oscillations in the emitted GS radiation.

4 DISCUSSION AND CONCLUSIONS

We performed 3D resistive MHD simulations of both a straight and curved kink-unstable twisted coronal loop using LARE3D. Both loops underwent reconnection, releasing stored magnetic energy, and exhibited broadly similar behaviour in terms of their energetics and internal dynamics. The GS emissions, observed in the microwave band, were forward modelled using a fast GS code developed by G. D. Fleishman & A. A. Kuznetsov (2010), similar to the approach used in C. Smith et al. (2022). The outcomes of our study are twofold. First, we have demonstrated a new methodology for analysing structural oscillations in a realistic model of a solar coronal loop, and used this to identify these. Secondly, we have explored the relationship between these structural modes and the associated local oscillations in plasma and magnetic field parameters, with oscillations in the GS emission light curves.

Using new methodology, we identified 'structural' oscillations of the loop (kink- and sausage-mode oscillations) by taking a cross-sectional slice of the loop-top, fitting an ellipse using Canny edge detection, Delaunay triangulation, and alpha shapes, and tracking the evolution of the loop-top's shape. We calculated the peak periods in the power spectra of these structural oscillations and compared them to peak periods observed in the emitted GS radiation, average twist, and internal parameters of the loop.

We identified sausage-mode and kink-mode oscillations in both loops. These oscillations shared similar peak periods, which were also observed in the oscillations of the loop's average twist. A potential reason for this is that a swaying loop, moving through regions of increased and decreased magnetic field strength, would lead to the loop-top periodically expanding and contracting. This would manifest as a sausage-mode oscillation and would also induce oscillations in the loop's average twist.

For the straight loop, a dominant period of approximately 222 s was observed in the oscillations of the GS emissions. Two similar peaks were also observed around 107 s. The 107-s period aligns with minor peaks found in the sausage-mode power spectra and oscillations seen in the internal parameters of the loop-top. The 222-s peak was not directly associated with any structural oscillation, which is expected due to the strongly non-linear relationship between radiative transport and radiative emissions. It was observed that the internal parameter oscillations and interference between observed sausage-mode oscillations give a period that aligns with the 222-s peak. Alternatively, other wave modes – undetected by the edge detection algorithm – could contribute to the emission oscillations. The approximately 83-s period observed in the structural and internal parameter oscillations did not appear in the GS emissions at all.

Similar conclusions can be drawn for the curved loop. The peaks in the GS emissions were observed at ∼233 and ∼527 s. The first peak overlapped with the 270-s peaks observed in the structural oscillations, indicating that, like the straight loop, one of the peaks in the GS oscillation is also driven by the sausage- and kink-mode oscillations. The dominant ∼526 s peak is not associated with any structural oscillations but could be associated with interference in the sausage-mode, kink-mode, and density oscillations. This suggests that for both the straight and curved loop, the GS oscillations could be generated by sausage- and kink-mode oscillations and interference of those modes.

A potential additional process was observed in the curved loop, affecting the oscillations in the loop's average twist. This oscillation had a period of approximately 119 s and could be caused by a torsional-like mode, which would induce oscillations in the average twist of the loop due to rotational motion around the loop-top.

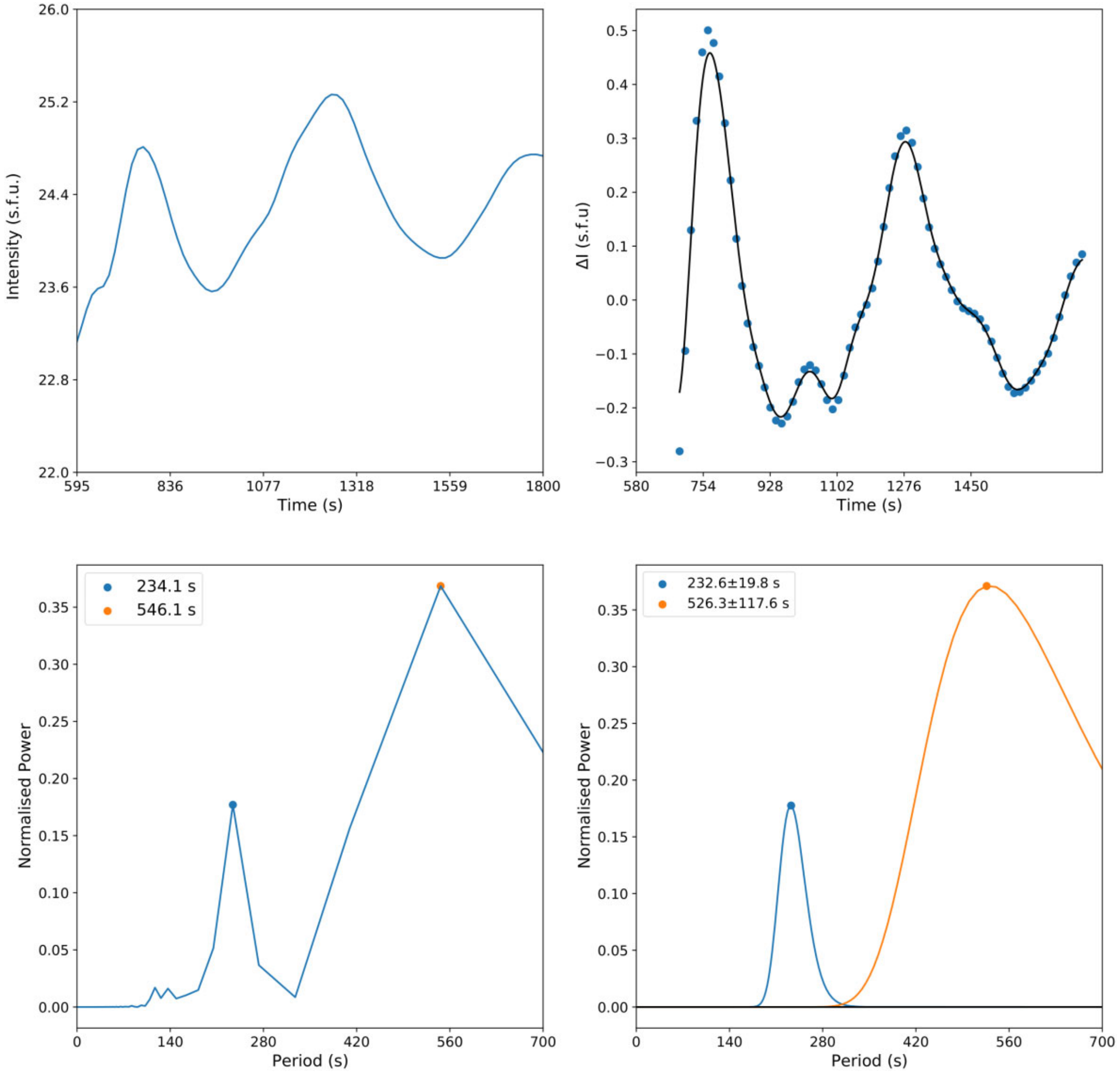

Figure 15. Analysis of the measured GS radiation at 15 GHz for the curved loop. The first row demonstrates how the GS radiation for each frequency evolves over time. The subsequent rows follow the same structure as in Fig. 9.

However, the 119-s oscillation did not appear in the GS radiation oscillations, suggesting that even if an additional mechanism was affecting the loop's twist, it did not contribute to the dominant period in the GS oscillations. Furthermore, in the straight loop, only one period was observed in the average twist oscillations, and this was shared with the periods observed in the kink- and sausage-mode oscillations. This suggests that there were no other mechanisms driving the oscillations in the average twist for the straight loop, discounting the potential contribution of a torsional-like mode for the straight loop as well.

In summary, both sausage- and kink-mode oscillations were detected in the straight and curved loop models. While these modes play a crucial role in shaping the GS emission – and thus any observed QPPs in the flare – the relationship between light-curve pulsations and underlying loop oscillations remains complex. This is not unexpected, due to the non-linear dependence of GS emission on the plasma and field parameters (G. Mossessian & G. D. Fleishman 2012; E. G. Kupriyanova et al. 2022; T. I. Kaltman & E. G. Kupriyanova 2023). Optically thick effects on the radiation may play a significant role in the relationship between the parameters in the emission regions and in the observed radiation. It is possible that the sausage- and kink-mode oscillations are the sole contribution to the GS oscillations, but it is also possible that mechanisms unidentified here play a role in determining the frequencies of the GS oscillations.

There is evidence to suggest that sausage- and kink-mode oscillations (and interference of these modes) may account for the GS oscillations emitted from the straight and curved loop model. While a torsional mode is unlikely to be responsible, other unidentified mechanisms could also influence their frequencies. In the curved case, curvature effects could introduce an acoustic mode.

Future research should investigate whether GS oscillations result from interference between sausage and kink modes or from another mechanism entirely. If the GS oscillations result from interference, it is important to gain a deeper understanding of how the sausage and kink modes interact, how this interaction translates into observable features of the microwave oscillations, and how variations in plasma parameters influence this behaviour. Deepening our understanding of these mechanisms not only increases our understanding of the time-dependent nature of solar flares but also paves the way for the development of seismological tools that could be used to determine plasma parameters within a flaring region from observed QPP data in the future.

ACKNOWLEDGEMENTS

We wish to thank the Science and Technology Facilities Council (STFC) for providing studentship support for JS. PKB and MG were funded by the STFC grant ST/T00035X/1. We also thank the Distributed Research utilizing Advanced Computing (DiRAC) group for providing the computational facilities used to run the simulations in this paper.

DATA AVAILABILITY

The data underlying this article will be shared on reasonable request to the corresponding author (JS).

REFERENCES

Agaian S., Almuntashri A., Papagiannakis A., 2009, in 2009 IEEE International Conference on Systems, Man and Cybernetics. IEEE, Piscataway, NJ, p. 3683

Altyntsev A., Meshalkina N., Mészárosová H., Karlický M., Palshin V., Lesovoi S., 2016, Sol. Phys., 291, 445

Arber T. D., Longbottom A. W., Gerrard C. L., Milne A. M., 2001, J. Comput. Phys., 171, 151

Archontis V., Hood A. W., Tsinganos K., 2013, ApJ, 778, 42

Bareford M. R., Hood A. W., 2015, Philos. Trans. R. Soc. A, 373, 20140266

Bareford M. R., Hood A. W., Browning P. K., 2013, A&A, 550, A40

Bareford M. R., Gordovskyy M., Browning P. K., Hood A. W., 2016, Sol. Phys., 291, 187

Benson D. J., Schoenfeld S., 1993, Comput. Mech., 11, 107

Benz A. O., 2017, Living Rev. Sol. Phys., 14, 2

Broomhall A.-M. et al., 2019, ApJS, 244, 44

Browning P. K., Van der Linden R. A. M., 2003, A&A, 400, 355

Browning P., Gerrard C., Hood A., Kevis R., Van der Linden R., 2008, A&A, 485, 837

Canny J., 1986, IEEE Trans. Pattern Anal. Mach. Intell., PAMI-8, 679

Caramana E. J., Shashkov M. J., Whalen P. P., 1998, J. Comput. Phys., 144, 70

Cargill P. J., Chen J., Garren D. A., 1994, ApJ, 423, 854

Chen B. et al., 2020, Nat. Astron., 4, 1140

Christensen R. B., 1990, Godunov methods on a staggered mesh: An improved artificial viscosity (LLNL Report No. UCRL-JC-105269 / DOE DE92011973). Lawrence Livermore National Laboratory.

Climent J. B. et al., 2022, A&A, 660, A65

Collier H., Hayes L. A., Yu S., Battaglia A. F., Ashfield W., Polito V., Harra L. K., Krucker S., 2024, A&A, 684, A215

Cozzo G., Pagano P., Petralia A., Reale F., 2023, Symmetry, 15, 627

De Moortel I., Nakariakov V. M., 2012, Philos. Trans. R. Soc. A, 370, 3193

Dominique M., Zhukov A. N., Dolla L., Inglis A., Lapenta G., 2018, Sol. Phys., 293, 61

Fan Y., 2009, ApJ, 697, 1529

Fleishman G. D., Kuznetsov A. A., 2010, ApJ, 721, 1127

Fleishman G. D., Bastian T. S., Gary D. E., 2008, ApJ, 684, 1433

Fleishman G. D., Nita G. M., Gary D. E., 2015, ApJ, 802, 122

Fletcher L. et al., 2011, Space Sci. Rev., 159, 19

Gary D. E., Hurford G. J., 1994, ApJ, 420, 903

Gordovskyy M., Browning P. K., Kontar E. P., Bian N. H., 2014, A&A, 561, A72

Gordovskyy M., Browning P. K., Kontar E. P., 2017, A&A, 604, A116

Hathaway D. H., 2010, Living Rev. Sol. Phys., 7, 1

Hood A. W., Priest E. R., 1979, Sol. Phys., 64, 303

Hood A. W., Priest E. R., 1981, Geophys. Astrophys. Fluid Dyn., 17, 297

Hood A. W., Browning P. K., van der Linden R. A. M., 2009, A&A, 506, 913

Hood A. W., Cargill P. J., Browning P. K., Tam K. V., 2016, ApJ, 817, 5

Hou X., Dong Y., Zhang H., Gu J., 2009, in 2009 Second International Conference on Intelligent Networks and Intelligent Systems. IEEE, Piscataway, NJ, p. 354

Inglis A. R., Ireland J., Dennis B. R., Hayes L., Gallagher P., 2016, ApJ, 833, 284

Kaltman T. I., Kupriyanova E. G., 2023, MNRAS, 520, 4147

Karampelas K., McLaughlin J. A., Botha G. J. J., Régnier S., 2022, ApJ, 925, 195

Karampelas K., McLaughlin J. A., Botha G. J. J., Régnier S., 2023, ApJ, 943, 131

Kontar E. P., Perez J. E., Harra L. K., Kuznetsov A. A., Emslie A. G., Jeffrey N. L. S., Bian N. H., Dennis B. R., 2017, Phys. Rev. Lett., 118, 155101

Kumar P., Cho K. S., Bong S. C., Park S.-H., Kim Y. H., 2012, ApJ, 746, 67

Kupriyanova E. G., Kaltman T. I., Kuznetsov A. A., 2022, MNRAS, 516, 2292

Kuznetsov A. A., Fleishman G. D., 2021, ApJ, 922, 103

Landshoff R., 1955, A Numerical Method for Treating Fluid Flow in the Presence of Shocks. Report, LA-1930, Los Alamos National Laboratory

Li D., Li Y., Lu L., Zhang Q., Ning Z., Anfinogentov S., 2020, ApJ, 893, L17

McLaughlin J., Moortel I. D., Hood A., Brady C., 2009, A&A, 493, 227

McLaughlin J. A., Verth G., Fedun V., Erdélyi R., 2012, ApJ, 749, 30

McLaughlin J. A., Nakariakov V. M., Dominique M., Jelínek P., Takasao S., 2018, Space Sci. Rev., 214, 45

Mathioudakis M., Seiradakis J. H., Williams D. R., Avgoloupis S., Bloomfield D. S., McAteer R. T. J., 2003, A&A, 403, 1101

Mathioudakis M., Bloomfield D. S., Jess D. B., Dhillon V. S., Marsh T. R., 2006, A&A, 456, 323

Meyer-Vernet N., 2007. Basics of the Solar Wind. Cambridge Univ. Press, Cambridge

Mishra S. K., Sangal K., Kayshap P., Jelínek P., Srivastava A. K., Rajaguru S. P., 2023, ApJ, 945, 113

Mitra-Kraev U., Harra L. K., Williams D. R., Kraev E., 2005, A&A, 436, 1041

Mossessian G., Fleishman G. D., 2012, ApJ, 748, 140

Nakariakov V. M., Verwichte E., 2005, Living Rev. Sol. Phys., 2, 3

Nakariakov V., Melnikov V., Reznikova V., 2003, A&A, 412, L7

Nakariakov V. M. et al., 2016, Space Sci. Rev., 200, 75

Nakariakov V. M., Kolotkov D. Y., Kupriyanova E. G., Mehta T., Pugh C. E., Lee D. H., Broomhall A. M., 2019, Plasma Phys. Control. Fusion, 61, 014024

Nita G. M., Fleishman G. D., Kuznetsov A. A., Kontar E. P., Gary D. E., 2015, ApJ, 799, 236

Parks G. K., Winckler J. R., 1969, ApJ, 155, L117

Phillips K. J. H., 1995, Guide to the Sun. Cambridge Univ. Press, Cambridge

Pinto R. F., Vilmer N., Brun A. S., 2015, A&A, 576, A37

Pinto R. F., Gordovskyy M., Browning P. K., Vilmer N., 2016, A&A, 585, A159

Priest E., 1982. Solar Magnetohydrodynamics. Cambridge Univ. Press, Cambridge

Reale F., Orlando S., Guarrasi M., Mignone A., Peres G., Hood A. W., Priest E. R., 2016, ApJ, 830, 21

Reale F., Lopez-Santiago J., Flaccomio E., Petralia A., Sciortino S., 2018, ApJ, 856, 51

Reid J., Hood A. W., Parnell C. E., Browning P. K., Cargill P. J., 2018, A&A, 615, A84

Rong W., Li Z., Zhang W., Sun L., 2014, in 2014 IEEE International Conference on Mechatronics and Automation. IEEE, Piscataway, NJ, p. 577

Shi F., Li D., Ning Z., Guo Y., Feng S., Xu J., 2023, ApJ, 958, 39

Shi M., Li B., Chen S.-X., Guo M., Yuan S., 2023, ApJ, 943, L19

Shibata K., Magara T., 2011, Living Rev. Sol. Phys., 8, 6

Smith C., Gordovskyy M., Browning P. K., 2022, MNRAS, 511, 2880

Snow B., Botha G. J. J., Régnier S., Morton R. J., Verwichte E., Young P. R., 2017, ApJ, 842, 16

Srivastava A. K., Zaqarashvili T. V., Kumar P., Khodachenko M. L., 2010, ApJ, 715, 292

Stewart J., Browning P. K., Gordovskyy M., 2022, MNRAS, 513, 5224

Takakura T., Kaufmann P., Costa J. E. R., Degaonkar S. S., Ohki K., Nitta N., 1983, Nature, 302, 317
Tam K. V., Hood A. W., Browning P. K., Cargill P. J., 2015, A&A, 580, A122
Thompson A. R., Maxwell A., 1962, ApJ, 136, 546
Thurgood J. O., Pontin D. I., McLaughlin J. A., 2017, ApJ, 844, 2
Thurgood J. O., Pontin D. I., McLaughlin J. A., 2018, ApJ, 855, 50
Titov V. S., Démoulin P., 1999, A&A, 351, 707
Török T., Kliem B., 2003, A&A, 406, 1043
Török T., Kliem B., 2005, ApJ, 630, L97
Török T., Kliem B., Titov V. S., 2004, A&A, 413, L27
Trucco E., Verri A., 1998, Introductory Techniques for 3-D Computer Vision. Prentice Hall, Upper Saddle River, NJ
van Doorsselaere T., Verwichte E., Terradas J., 2009, Space Sci. Rev., 149, 299
van Doorsselaere T. et al., 2020, Space Sci. Rev., 216, 140
Vernazza J. E., Avrett E. H., Loeser R., 1981, ApJS, 45, 635
Vidotto A. A., 2021, Living Rev. Sol. Phys., 18, 3
Von Neumann J., Richtmyer R. D., 1950, J. Appl. Phys., 21, 232
Waterfall C. O. G., Browning P. K., Fuller G. A., Gordovskyy M., 2019, MNRAS, 483, 917
Zaqarashvili T., Melnik V., Brazhenko A., Panchenko M., Konovalenko A., Franzuzenko A., Dorovskyy V., Rucker H., 2013, A&A, 555, A55
Zimovets I. V. et al., 2021, Space Sci. Rev., 217, 66

This paper has been typeset from a TEX/LATEX file prepared by the author.